AN ABSTRACT OF THE THESIS OF

Austin Berrier for the degree of Master of Science in Mechanical Engineering presented on June 7, 2021.

Title: Design Optimization of a Structurally Flexible Wave Energy Converter with a Direct Search Algorithm

Abstract approved: _____

Bryony L. DuPont

Several wave energy converter designs have been recently proposed that are made of flexible materials. Flexible devices are able to generate electricity by being stretched, and are intended to simplify deployment and maintenance concerns over existing wave energy devices. Due to the relative infancy of flexible wave energy converters, however, little is known about how to optimally design one for its deployment location. We chose here to optimize a long flexible tube, a seemingly straightforward design nonetheless having a large design space including geometry, submergence, material, and mooring considerations. A brute force search of all these factors would take engineers an impractical amount of time to completely explore, so we used a direct search optimization algorithm to explore potential design concept changes and exploit those that result in an overall improvement. We focused on the geometry and submergence of the flexible device with fixed mooring and material parameters, and successfully used the device's overall power performance as our metric for improvement. We intend our optimization work to be a case study in using design automation and optimization methods to improve other flexible wave energy devices.

Design Optimization of a Structurally Flexible Wave Energy Converter with a Direct Search Algorithm

by

Austin Berrier

A THESIS

submitted to

Oregon State University

in partial fulfillment of
the requirements for the
degree of

Master of Science

Presented June 7, 2021
Commencement June 2022

Master of Science thesis of Austin Berrier presented on June 7, 2021.

APPROVED:

Major Professor, representing Mechanical Engineering

Head of the School of Mechanical, Industrial, and Manufacturing Engineering

---

Dean of the Graduate School

I understand that my thesis will become part of the permanent collection of Oregon State University libraries. My signature below authorizes release of my thesis to any reader upon request.

Austin Berrier, Author

ACKNOWLEDGEMENTS

Thank you to so many wonderful and kind folks who have generously helped me along the way: Elise and Andrew. Phoebe. My parents and step parents, especially my mother. Jake Light, Ellie Dunkle, and Michelle Nguyen. Jess, Corinne, and Jack. Matt Johnson and Randeep Baweja. Aeron Roach, Michael Devin, Mel Ellis, and Naser Alqseer. Ali Trueworthy and Hannah Mankle. Tyler Inkley, Jill Light, and Matt Leary. Justin, Travis, and Griffin. The many students of ME 382.

Bryony DuPont, Mike Lawson, and Yi-Hsiang Yu for mentoring me and trusting me to independently follow my research interests this past year. Jennifer van Rij for providing helpful starting code, comments, and hydrodynamic simulation files for simulating a flexible wave energy device. Chris Hoyle and Matt Campbell for help with my optimization work, especially Chris for getting me started and interested in both Bayesian and robust design optimization. Bryson Robertson for bringing me to Oregon State, being generous in letting me use his computational resources and helping me along the way, and keeping the Pacific Marine Energy Center floating along in the right direction. Melanie Fewings for encouraging a healthier approach to work and life, and showing me what the future of academia can look like. Barbara Simpson for help with modal analysis. Kyle Niemeyer for funding my first winter term of graduate school and letting me get my toes wet in computational fluid dynamics. Andy Dong for being a fantastic school and head and professor to work for. Jason Ideker for serving as my Graduate Council Representative. Ryan Coe and Jonathan Boreyko for encouraging my work and interests, and for all the advice too.

You're all wonderful - here's to a better world.

This thesis research was supported by an appointment with Marine and Hydrokinetic Graduate Student Research Program sponsored by the U.S. Department of Energy (DOE), Office of Energy Efficiency and Renewable Energy, and Water Power Technologies Office. This program is administered by the Oak Ridge Institute for Science and Education (ORISE) for the DOE. ORISE is managed by ORAU under DOE contract number DESC0014664. All opinions expressed in this paper are the author's and do not necessarily reflect the policies and views of DOE, ORAU, or ORISE.

TABLE OF CONTENTS

TABLE OF CONTENTS (Continued)

LIST OF FIGURES

Figure Page

LIST OF FIGURES (Continued)

Figure Page

LIST OF FIGURES (Continued)

Figure Page

[The sea] is my favorite thing, I think, that I have ever seen...It seems big enough to contain everything anyone could ever feel.

Anthony Doerr

-

Chapter 1: Introduction

1.1 Flexible Wave Energy Converters

Commercial wave energy projects consist primarily of designs that generate power from rigid body motion along a single degree of freedom. These designs typically resonate naturally only at a single incident wave frequency, and so require passive or active on-board control strategies to tune their rigid body motion for resonating at other frequencies. Control strategies come at the cost of additional system complexity, however, and can inherently lead to potentially high motion amplitudes or component forces on the hull or internal power conversion system. Fracture of these components in particular can be catastrophic for an offshore structure, potentially leading to being taken entirely out of service.

To address the inherent limitations of these rigid body wave energy systems, some developers and researchers have recently proposed several different wave energy converter designs that are made of flexible materials. Flexible designs include variants of their rigid body counterparts, including oscillating surge devices [1], attenuators [2], heaving point absorbers [3], and oscillating water columns [4]. Another notable device includes the Anaconda, which uses traveling deformation waves to harness power at its end [5]. Flexible devices build their power conversion system directly into the hull, and are able to extract power from their environment just by being stretched. We mathematically treat flexible devices as continuously deformable structures over both space and time, and we call the functions that describe the shape a flexible system moves in its mode shapes. Each of these mode shapes corresponds to its own natural frequency as well, which means that a flexible wave energy structure can resonate simultaneously at multiple wave frequencies corresponding to its environment. The natural frequencies of any system are a function of its geometry as well as material and mooring parameters, meaning that a system's natural frequencies can be tuned to its environment by altering these parameters. The shape a given designed device takes on in its environment is then a linear sum of its mode shapes. Each resonant mode shape is able to dissipate its own

amount of power due to the amount of deformation present, and also depends on how much internal and controlled system damping is present. Considering these complexities, it is a nontrivial task to explore the optimal design parameters to improve the electrical power production of a device, a typical metric used for offshore renewable energy design analysis and optimization. Evaluating a single flexible wave energy converter using linear methods can still be computationally time intensive too, meaning that methods typically used for optimizing rigid body wave energy devices cannot be practically used.

1.2 Outline of Work

Wave energy converter design optimization is typically performed using a set of geometry parameters to assess a device. The algorithm used to optimize a device can be pragmatically based on the required time to evaluate each design's objective, as well as the number of design variables and search space complexity. For example, Blanco et al. and Mankle et al. both studied optimizing the radii and drafts of a two-body heaving cylinder model [6, 7], while both McCabe [8] and Garcia-Teruel and Forehand used a genetic algorithm to improve the hydrodynamic design of a device using defined bicubic surfaces [9]. We study here optimizing the geometry and submergence a flexible tube similar to that being developed by SBM Offshore, Inc., and built out of a dielectric elastomer generator material [10]. The material itself combined with power electronics can be used to convert power directly from wave induced mechanical deformations [11], and can be seen as the flexible equivalent of a rigid body attenuator design.

We chose here to optimize a long flexible tube, a seemingly straightforward design that nonetheless has a large design space including geometry, submergence, material, and mooring parameter considerations. A brute force search of all of these factors and their relationships would take engineers an impractical amount of time to completely explore, so we used two different direct search optimization algorithms to explore and exploit every potential design improvement for us. We used each algorithm to optimize an average power performance metric of a flexible WEC being deployed at Humboldt Bay, California. Improving a design with automation methods requires us first to parameterize it, or pick a set of variables that completely describe it. These parameters include its geometric length and radius, its mean submergence, its material elasticity and internal fiber pretension, and its mooring line stiffnesses.

To evaluate a design, we first use a given set of design parameter values to determine the tube's natural frequencies. Each natural frequency corresponds to a particular device mode shape, or a way the tube will naturally deform, and each mode shape looks like an outward sine or cosine wave. We then use linear wave theory to solve for how difficult it is for each natural mode shape to be excited. Higher excitability and a lower resistance to movement across multiple wave frequencies mean that a design will perform well. Solving for how excitable a single mode is requires anywhere from 1 to 30 minutes of computational time, so we are practically limited by this time requirement in how many total designs we can evaluate over the course of the optimization. After evaluating how excitable each mode is, we tune how much we dampen every mode in order to maximize the tube's capable mean power output. Not enough damping means that we can obtain more power, and too much damping means that the tube is unable to deform a useful amount. After evaluating a given set of design parameters or values, we repeat the evaluation process for a new set of design values. If the new values lead to a higher mean power than the previous values, and we keep this design change. If it performs worse, we choose a different set of values and try again. In this way, by keeping only changes that cause improvements, we can explore a large set of different designs in a relatively efficient manner. When no even small changes can be made to a given design without it getting worse, we consider our algorithm to be converged and have found the optimal set of design parameters.

Chapter 2: Evaluating and Designing for Wave Energy Converter Structural Loads

2.1 Reducing Wave Energy Costs

Global warming has already dramatically affected our world, and will continue to negatively impact environmental and human health [12] as long as nation-states emit greenhouse gases at unsustainable rates. Numerous social and technical methods are necessary to decrease anthropogenic greenhouse gas emissions, such as lowering per capita resource usage, electrifying transportation, and switching electricity to come from renewable energy sources [13]. One recently promising form of renewable energy to fill a portion of global electricity demand is ocean wave energy, which directly converts the motion of a floating or submerged wave device into electricity. For example, ocean waves off the United States' coast have the ability to power 30% of the country's annual electricity usage [14]. In addition to providing electrical power directly to an onshore utility scale grid, ocean energy can also be used for potential applications in ocean observing, underwater vehicle charging, marine aquaculture, desalination, disaster recovery, and powering microgrids for geographically isolated communities [15].

However, despite government backing in multiple countries, no wave energy converter developer to date has launched a commercially active wave energy array project, and multiple companies have bankrupted. G. Chang et al. used numerical simulations to demonstrate that pilot-scale device arrays for multiple WEC types were able to produce electricity at levelized costs of energy between \$0.37 and \$1.22/kWh. In order to lower their cost of energy production to a more competitive value of \$0.30/kWh or below, the authors found that companies would be required to lower capital and operating expenditures by at least 45% [16]. One potential way to lower expenditures is by reducing structural and operations costs, which are respectively estimated to be 36 and 28% of total project costs [17] and can depend on the size of a device array [18]. Paredes et al. also presented a cost breakdown for a floating oil production unit off the coast of Norway, which had structural and operational costs respectively at 4 and 81% of total

costs [17]. This large difference in cost percentage breakdowns shows that structural design improvements in WEC design can lead to a more significant system cost reductions than could necessarily be anticipated for other offshore systems.

Improving structural load evaluations can lower the need for excess design safety factors, reducing long-term capital and operating expenditures [19]. Various array simulations have directly demonstrated that improving component reliability can increase project profitability [20] as well as lower the expected value and variability in levelized energy production costs [21]. Component and system failure rates can be reduced as well, thereby increasing operational times and reducing component replacement costs [22]. Astariz and Iglesias divide WEC systems into four sub-systems for failure rate estimation purposes: structural, power take off, mooring, and power transmission systems [23]. We intend our review as focusing on WEC structural components without considering any external mooring or cable connections.

Due to the marine energy industry's relative infancy, there is fairly limited data in the literature on actual WEC failure causes during live ocean testing. Outer shell damage on a Wavestar prototype's float caused two months in operational downtime [24], and operation of the Wave Dragon overtopping WEC caused failures at connections between fenders and the main hull [25]. While hull structure failure probabilities have been estimated to be 0.0066 per year, they can require 72 person hours to repair [26].

As to power take off (PTO) failure in industry, Astariz and Iglesias estimated component failure rates for hydraulic components to be as high as 0.24 for the ram and 0.42 for the accumulator, and 1.59 for the electric generator [23]. More work needs to be done to successfully predict loads on these components to lower failure rates and increase deployment lifetimes.

2.2 Evaluating Hydrodynamic Loads

In order to adequately design an offshore structure, we first need to analyze the forces acting on it. Fatigue stresses due to cyclic loading should be considered on hull and PTO components. In addition, for floating devices, it is necessary to calculate concentrated loads due to events such as slamming.

Long term loading is complicated by the fact that design considerations of wave energy converters is typically different from other offshore structures. Wave energy converter

structures and control algorithms are typically designed to achieve resonance rather than preventing it. Because of this, we are interested both in the natural frequencies both of the rigid body structure of the device to achieve resonance, and of the structural frame in order to typically prevent resonance. Evaluating natural frequencies is one of many steps in evaluating the design loads on a device under consideration.

High-fidelity short term design load assessments can be made using fully nonlinear methods, such as coupled computational fluid dynamics and finite element structural analyses. However, nonlinear fluid structure interaction simulations are computationally more expensive than potential flow theory by 6 to 12 orders of magnitude [27], and so are generally infeasible for assessing long term design loads on an entire structure [28] or incorporation into initial design work or optimization. The focus of my review is on using linear potential flow theory to assess design loads for a wave energy converter's hull and power take off systems.

Potential flow models can be used in both the frequency and time domain, and can be respectively considered as low- and mid-fidelity models for predicting WEC loads [29].

The mathematical bases and assumptions for using potential flow theory in both frequency and time domains are given below.

Potential flow theory has a mathematical basis in assuming an inviscid flow in order to convert the Navier Stokes equations into the Euler equations. Treating the fluid as incompressible (2.1) and irrotational lets us define a potential function whose negative gradient is the velocity of the flow (2.2). Equations (2.1) and (2.2) are combined to produce the Laplace equation (2.3) for the fluid potential over the domain. Assuming small wave amplitude and steepness then allows linearizing the free surface boundary conditions in order to solve for fully linear solutions of the fluid potential over the domain [30].

$$\nabla \cdot \mathbf{u} = 0 \tag{2.1}$$

$$\mathbf{u} = -\nabla\phi \tag{2.2}$$

$$\nabla^2\phi = 0 \tag{2.3}$$

The fluid potential function has to be solved for numerically by discretizing the submerged surface into a mesh to convert the solution process into a linear system of complex

valued equations [31]. Various boundary element methods have been implemented to automatically create the required matrices and solve them, such as Capytaine [32], Nemoh [33], and WAMIT [34]. The linearity of the problem allows solving for the wave radiation potential ϕ_R and diffraction potential ϕ_D separately (2.4) due to a harmonic incident wave potential ϕ_I, and to treat each rigid body motion independently as well [35].

$$\phi = \phi_D + \phi_R + \phi_I \tag{2.4}$$

After solving for the potential at each mesh cell, a linearized Bernoulli's equation can then be used to calculate pressure forces [36]. These pressures are then spatially integrated in order to calculate frequency dependent excitation force $F_e(\omega)$, as well as added mass $A(\omega)$, damping $B(\omega)$, and linear hydrostatic restoring stiffness K. These terms are used in the device equation of motion in any rigid body direction, listed below for a device with rigid body mass m moving in a single degree of freedom with position x, velocity $\dot{x}$, and acceleration $\ddot{x}$:

$$(m + A(\omega))\ddot{x} + B(\omega)\dot{x} + Kx = F_e(\omega) \tag{2.5}$$

Response amplitude operators (2.6) can additionally be defined from these coefficients that relate the motion of a device in a specified degree of freedom to the incident wave amplitude [37, 38]:

$$RAO(\omega) = \frac{F_e(\omega)}{-\omega^2(m + A(\omega)) + i\omega B(\omega) + K} \tag{2.6}$$

Response amplitude operators effectively act as transfer functions that show a device's linear response to an incoming wave, and can be seen in the literature as the shorter abbreviation $H(\omega)$ as well. That is, a device will have a steady state response amplitude equal to:

$$A|H(\omega)|\sin(\omega t + \phi + \epsilon) \tag{2.7}$$

Where A is the incoming wave amplitude, ϕ the phase angle of the response, and ϵ a phase angle that is zero valued for a regular wave and randomly valued from 0 to 2π for a component of an irregular wave spectrum.

Taking the inverse Fourier transform of the frequency domain equation of motion [37]

leads to the Cummins equation [39] in the time domain, shown below in (2.8):

$$(m + m_\infty)\ddot{x} = -\int_{-\infty}^{t} K(t-\tau)\dot{x}(\tau)\, d\tau + F_e - F_{hs} + F_{ext} \tag{2.8}$$

Here, m refers to the rigid body mass of the device, m_∞ refers to its added mass value at infinite frequency, and $\ddot{x}$ refers to the acceleration vector of the device. The forces on the right hand side respectively refer to the wave radiation, excitation F_e, hydrostatic F_{hs}, and any additional external forces F_{ext} such as viscous, power take off, or mooring loads [29]. The convolution integral term used to calculate the radiation force is computationally expensive to directly calculate, and so can be handled instead by using a state space approach to approximate it [37, 40]. Additional methods for solving the radiation force are discussed in Armesto et al. [41].

As discussed previously, due to its underlying mathematical assumptions, using potential flow theory is limited to small motions due to waves with small wave amplitudes and steepness in order to decouple rigid body and elastic responses in each degree of freedom. However, calculating accurate restoring Froude-Krylov forces in the heave direction also depends on the geometry of the device. This is because the linear stiffness of the device is calculated as directly proportional to the average submerged surface [42]. For devices with a constant cross sectional area such as a cylinder, Retes et al. found that linear restoring forces were accurate as long as the device was never fully submerged or out of the water (i.e. their cross sectional area changed). However, for devices with changing cross sections, device motions on the same order of magnitude as the device's draft were enough to obtain inaccurate device motion [43].

2.3 Assessing Linear WEC Hull Loads

2.3.1 Frequency Domain

Wave energy converters encounter environmental loads due to their short-term wave environment as well as long-term drift forces, and need to be designed for both reliability and survivability in long deployments. This section of my review focuses on evaluating loads on wave energy converter hulls. In wave energy. we typically only evaluate rigid body responses due to incident waves. For a rigid body motion, the entire device moves

or rotates along a degree of freedom in a given direction, say a heave direction for a barge. We can think of a beam deflecting with a uniform value to be equivalent to a heave motion, or a linear deflection to be a pitch motion. Or we can have the ends of the beam stay stationary and bend in the middle. This creates a deflection amount as a function of x. We can make this even more general by having deformations be functions of x, y, and z, by example for a radially deforming tube.

For generalized body modes analysis, we generalize this to have parts of the structure move relative to one another. In this way, the body movements are actual functions of the location on the body instead of a uniform movement.

Most work to date on evaluating hull structural loads have been performed using generalized body modes analyses in the frequency or time domain using potential flow formulations. In generalized body modes analysis, structural deflections can be treated in terms of elastic modal shapes that depend on the geometry and boundary conditions of the structure [36]. Generalized body modes analysis treat elastic deformations as independent degrees of freedom without any cross-coupling, so the rigid body dynamics of the structure can be treated as decoupled from its structural response. Modal responses are first input into and calculated in the frequency domain using boundary element modeling tools, and then can be transferred to the time domain using Cummins' equation.

The procedure for finding hull structural responses using generalized body modes analysis is as follows:

1. Define the structure's body modes using analytical theory, finite element analyses, or arbitrary functions.

2. Calculate the modal mass $\boldsymbol{M}$, stiffness $\boldsymbol{K}$, and damping matrix $\boldsymbol{B}$ for all modes.

3. Determine the hydrodynamic response for each mode using a boundary element method at all incident wave frequencies of interest.

4. Use matrix algebra to calculate the response amplitude operators $\hat{a}$ for each mode shape.

5. Assess the total material response due to summing each modal response.

6. Convert deflections to material stresses using engineering analyses such as beam or plate theories, or finite element analysis.

7. Use statistical methods to form a probability distribution of expected long term wave loads.

The body mode shapes of a wave energy converter correspond to the way its underlying structure wants to naturally move, and can be defined in a number of different ways. Bending mode shapes typically appear as elements of cosine or sine waves for a long floating body. Newman [36] and van Rij et al. [27] both used analytical Euler-Bernoulli beam modes for a floating barge (free-free beam) and a surface piercing column that extended to the seafloor (fixed-free beam). Analytical modes are found for simple geometries by solving the beam or plate equation for a given set of boundary conditions. Modes can often be used to directly evaluate the natural dry frequencies of the structure.

Modes are often simplified by treating the body as a one-dimensional system. Floating barges were treated as a free-free beam and a bottom mounted beam was treated as a cantilever. Newman also investigated how using different modal shapes affected the barge's computed bow bending response. Instead of using analytical modal shapes, the author used both Legendre and Chebyshev polynomials, both mode shapes that do not satisfy beam boundary conditions. They found that using arbitrary mode shapes did not affect the converged bending response at the bow, but noted that achieving similar convergence to the use of analytical modes required using additional problem degrees of freedom and therefore computational time. Van Rij et al. used a lumped mass Rayleigh-Ritz approach to calculate one axial displacement and bending modal shape each for a Reference Model 3 [44] two body point absorber, which has a more complex mass distribution and therefore modal response than a uniform beam. The authors represented the structure as a beam with two lumped masses for its float and heave plate at their respective mass centers, and two external springs for linear restoring mooring forces [29].

Modes have been analytically derived for WEC structures made of elastic materials as well. Babarit et al. lists the modal shapes for a fixed bottom pressure differential WEC with air chambers [45]. Chaplin derived the mode shapes for a submerged flexible tube called the Anaconda [5]. Babarit et al. derived and list the mode shapes for a similarly shaped flexible tube, albeit with different boundary conditions from the Anaconda [46].

Modal responses outputted from boundary element method tools additionally depend on the inertial, damping, and stiffness matrix terms corresponding to each structural mode.

Most works assessed modal mass and stiffness values using analytical one-dimensional integrals along the primary length dimension of the structure [27, 36, 47, 48]. McDonald et al. lists modal mass, damping, and stiffness matrix surface and volume integrations for membrane membrane WECs with Wells turbine and dielectric elastomer generator power take off systems [49].

For most relatively stiff devices, modal damping was not considered [29, 50, 51]. However, one work found it necessary to introduce a modal damping term for an elastic column by using a linearized drag with an equivalent linear damping term. Without considering modal damping, the structural response amplitudes were unrealistically higher than those find using high-fidelity methods [27]. Taghipour et al. assigned system damping to be 1% of critical damping [47]. Scriven et al. used Rayleigh damping to approximate the full damping matrix for a finite element model, which assumes that structural damping is the sum of proportionality constants multiplied by element mass and stiffness matrices [52].

2.3.2 Time Domain

Modal responses for elastic degrees of freedom can then be simulated in the time domain using Cummins' formula (2.8), or the semi-empirical Morison equation. If using the Cummins' formula, you can use a rainflow counting technique to calculate accumulated fatigue damage over time.

Morison's equation integrates a sum of inertial and drag forces over the height of a simple bottom mounted column structure in order to calculate sinusoidal total system forces [30]. Ambühl et al. used this method to calculate foundation forces and moments, and introduced a model uncertainty factor to its results for using linear instead of nonlinear theory [53]. Singh et al. used the Morison equation as well to calculate maximum loads on a Wavestar type device, then used maximum found loads as input to a static structural finite element analysis on a full scale platform [54]. The Cummins equation has been used to simulate structural loads and displacements in an oscillating surge device with passive damping by coupling WEC-Sim [55] to the finite element code Code_Aster. WEC-Sim was used to calculate pressure loads that were input to the finite element model, which was then used to calculate the resultant device and PTO state to be passed back to WEC-Sim. This method is known as two-way loose coupling because the solutions

are calculated separately from one another. The authors of this work lead found that introducing structural and hydrodynamic model coupling increased both peak and root mean square PTO loading by 11% when compared to using only rigid body PTO loading results from WEC-Sim [52].

2.3.3 Limitations

Responses calculated using generalized body modes in either the time or frequency domain assume small deformations [45, 46] and small wave amplitudes. This assumption generally holds for relatively rigid WECs with small material strains relative to the rigid body motion. This should be treated with caution for elastic devices such as SBM Offshore's S3, however, which is designed to expand in cross sectional area between 10 and 50% [56]. The theory is limited too by a lack of work in achieving accurate response convergence at engineering points of interest for structures with more geometric complexity beyond simple algorithms. By comparing results with fully nonlinear fluid structure interaction methods, [27] found that using only one generalized body mode was generally accurate to find material stresses in simple barge and column geometries. However, this same methodology was found by [29] to be insufficient to calculate accurate forces in a more complex structure.

2.4 Assessing WEC Power Conversion System Loads

WEC power conversion systems, also called power take offs (PTOs), are responsible for converting absorbed mechanical power to electrical power, and can reside on or off of the device hull. Some PTO systems are made of hydraulic components for heaving or surging devices, or use a Wells turbine for oscillating water columns.

Research on improving WEC performance with existing designs has focused on finding active PTO control algorithms to improve device performance, a particularly relevant goal for point absorbers due to their narrow resonance bandwidth [57]. Device control can be categorized into: actively altering the PTO force, changing the device's geometry, and regulating the system's electrical output [58]. Hong et al. have reviewed electrical control strategies for WECs [59] and multiple reviews exist that cover mechanical control strategies relating to power production, so we only discuss control strategies relating to

structural loading here.

PTO component loads can only be assessed by assuming a control strategy for the system to implement. A reactive system controller means that there is a two way connection between the PTO and generator, allowing the generator to supply power back to the PTO and tune the device's motion to the current wave climate. In contrast, a passive controller can only absorb power from the device and cannot return any power back to the system.

Two commonly used WEC controller types are linear resistive and complex conjugate controllers, which respectively maximize a linear device's absorbed mechanical power for passive and reactive PTOs [57, 60]. Garcia-Tereul and Forehand [9] and Clark et al. [61] both used a complex conjugate controller to calculate the PTO force history for a set of wave frequencies, then linearly added each PTO frequency component as a harmonic forcing function with random phase shifts. Clark et al. then used the time domain PTO forcing along with Palmgren-Miner's rule to calculate fatigue loading at a weld connecting the WEC's floater and PTO. Edwards et al. used optimal linear resistive damping with an assumed zero valued PTO stiffness to assess three hour PTO design loads along various 100 year environmental condition contours [62]. The authors simulated PTO loading in the time domain using WEC-Sim coupled with the lumped mass mooring code MoorDyn [63], and found that PTO response statistics depended on the contour method used. Nguyen et al. used polynomial chaos expansion to create a reduced order model of long term PTO extension and force for an oblate spheroid point absorber [64].

Using a complex conjugate controller has a number of practical limitations. First, implementations are non-causal, meaning that they require future velocity information to implement in the time domain [65]. The controller type is also constraint free and maximizes absorbed mechanical power without regard to PTO efficiency [66]. Not incorporating constraints into the controller increases absorbed mechanical power at the expense of increasing PTO forces and WEC motion. Assuming a lossless PTO also means that the control force this method implements is not necessarily optimal, as maximizing absorbed mechanical energy is not necessarily equivalent to maximizing electrical output. However, PTO efficiency can depend on PTO force and system speed and therefore should not necessarily be treated as a constant value across all loading conditions [67].

Much work has been done to study optimal real-time WEC control with various

constraints or forcing function types, including latching controllers [68], model predictive control [69], fuzzy logic controllers [60], optimal velocity tracking [70], and reinforcement learning methods [71]. Of these, most study using continuously variable control, and relatively few works have studied resulting PTO loading statistics and fatigue damage on components. However, real WECs often implement PTO forces at a set of discrete times rather than continuously, as seen in the hydraulic PTOs in the Pelamis [72] and the Wavestar [73]. Hansen et al. specifically found that implementing a discrete displacement controller risked exciting structural natural frequencies [73], which could in turn cause unwanted loading.

When considering reactive controllers, Yang et al. used a latching PTO controller to study abrasive wear on PTO hydraulic components in a single sea state [74]. Ferri et al. studied how different maximum energy control algorithms applied to the same Wavestar device affected design requirements due to structural fatigue [75]. They found that switching from a passive to an actively controlled device increased absorbed power by a greater amount than the corresponding required material addition to device components. PTO constraints can be explicitly treated in the optimal control problem using methods such as a pseudo spectral approach, resulting in a constrained complex conjugate controller [65, 76]. These methods typically aim to maximize absorbed mechanical power while satisfying PTO displacement, velocity, or force constraints. PTO loading can also be incorporated directly into the objective function of a control algorithm to aim for a balance between increasing absorbed power and lowering structural forces. Tom et al. used this approach with a psuedo-spectral optimal control method to balance structural surge foundation loading with maximizing captured power [76]. They found that this reduced structural loads by a greater proportion than the subsequent drop in mechanical power.

Though the subject of this review is limited to low- and mid-fidelity modeling, which should not be used to evaluate design loads in extreme wave events due to modeling nonlinearities [42], it is still of interest to discuss geometry control methods used to control structural loads. Although it is not possible to directly know the combinations of significant wave heights and energy periods that cause the highest hydrodynamic and structural loading [77], some works consider exceedances in just significant wave height to be responsible for device survivability conditions [24]. A further complication to WEC survivability is that unlike wind turbines, which can turn and pitch their blades to get

out potentially hazardous wind conditions [78], it is impractical to consider removing any type of moored wave energy device from the water in extreme conditions. Ringwood [35] considers this with expressing that,

> [O]nce the wave excitation exceeds a certain level, there may be no control solution (for the PTO force) that simultaneously satisfies force and displacement constraints...If no viable control solution is available, the PTO must be locked, or the device must enter some form of survival mode, if structural damage is to be avoided.

Various survival modes have been implemented by developers to address this, such as the Wavestar being able to raise its floats out of the water in excessive significant wave heights [24]. Mundon and Rosenberg considered several different survivability strategies for their Triton two-body multi-mode WEC, characterizing four analysis statistics to allow for comparisons: mooring slack line frequency, drivetrain travel (in order to reduce end stop impacts), tendon loading, and mooring loading [79] . The authors ultimately found that the best design option was to lower excitation forces by ballasting their device to a depth of 10 m. Stallard et al. found that the top surface of a WEC could be designed to limit an axisymmetric float's hydrodynamic response [80]. This result directly shows that device survivability can incorporated at initial device stages instead of assessing survivability for a set design.

2.5 Future Work

Work on evaluating accurate WEC structural loads for complex designs is just beginning. It is also possible that new methods not discussed above could be used to assess structural fatigue on WEC components, such as semi-empirical frequency domain tools [81]. Similar methods have been used to assess structural loads for wind turbines [82], and use moments of a spectral stress density curve to directly estimate a probability density function of expected stress responses and ranges [83, 84].

Most research to date has focused on evaluating power take off load response statistics and uncertainties, including environmental contour methods and reduced order models such as polynomial chaos expansion. These methods can be directed applied to study long-term structural loads as well. Work can be done for more complex devices to di-

rectly compare generalized body modes analysis loads to more computationally expensive nonlinear models. In addition, few works have studied using device geometry to directly control device responses and structural forces in either expected or extreme sea states. All of this work, especially reduced order structural force and fatigue assessments, can be directly combined with constrained optimal control algorithms to obtain faster estimates of entire system loading and fatigue damage accumulation. WEC design optimization can then be used to directly study system tradeoffs between designs' estimated power and structural loading, showing considerable potential for potential flow methods to lower project development costs.

Chapter 3: Methods

3.1 Design Assessment

Wave energy converter design optimization is typically performed using a set of geometry parameters to assess a device. The algorithm used to optimize a device can be pragmatically based on the required time to evaluate each design's objective, as well as the number of design variables and search space complexity.

We outline here the automated process used to assess each set of flexible tube design variables $\vec{x}$. The geometry of each tube can be completely described by its static radius r_s and length L. Each tube is modeled as a thin cylinder with thickness t and end caps, as described in Ancellin et al. [85]. Its spatial location is described by its submergence z_s and pitch angle θ_p if we locate it at 0 degrees relative to incident waves, although we consider only a horizontally oriented tube here ($\theta_p = 0$).

We quantify each concept's performance by its expected annual power output at Humboldt Bay, California. Each function evaluation time takes an extensive amount of time (5 minutes up to 2 hours), so we prioritize obtaining an improved design in as few iterations as possible. We do this by making discrete search step sizes $\vec{d}$ in the design space $\vec{x}$ that get progressively smaller over each optimization run, which is known as a Hooke and Jeeves type algorithm [86]. In this way, we can obtain an improved solution in less than approximately 50 total iterations.

3.1.1 Design Variables

The following is a vector of design variables in the search space of our optimization problem:

$$\vec{x} = [r_s, L, z_s]$$

Where r_s, L, and z_s are the static radius, length, and average submergence of the tube.

Each search variable was given lower and upper bounds as follows, along with an appropriate resolution, or step size in the search space:

Variable $\in$ [Bounds]	Smallest Step Size
$r_s \in [0.05, 3.0]$ m	0.05
$L \in [20, 200]$ m	2
$z_s \in [-12.0, 3.0]$ m	0.25

We chose the lower bounds, upper bounds, and step sizes for each design variable by allowing each to have a reasonably large number of possible values (approximately 50-100 steps) while also allowing a fine enough resolution to give a meaningful optimal solution, and inspired by a preliminary study into the area [87]. Each set of geometry and bounds is wide enough to contain the geometry studied by [85] and a 10 times Froude scaled version of [48]. The step sizes denote a possible design change direction $\vec{d}$, and are used to create a new design x_{new} relative to the current design $\vec{x}_c$:

$$\vec{x}_{new} = \vec{x}_c + \alpha\vec{d}$$

Where α is a step size parameter that decreases in magnitude over the course of the optimization. Because the list of potential search directions $\vec{d}$ is user generated and fixed over the course of the optimization, this is known as a pattern search This enables large design changes to happen at the beginning of the optimization without many evaluations, and smaller steps to occur later on to fine tune the optimal design.

3.1.2 Constants

Values listed in the following table are constant for each tube design for all design optimizations. All tube material constants are found from [48] or a Froude scaled version of the tube in [85] scaled by a factor of 10.

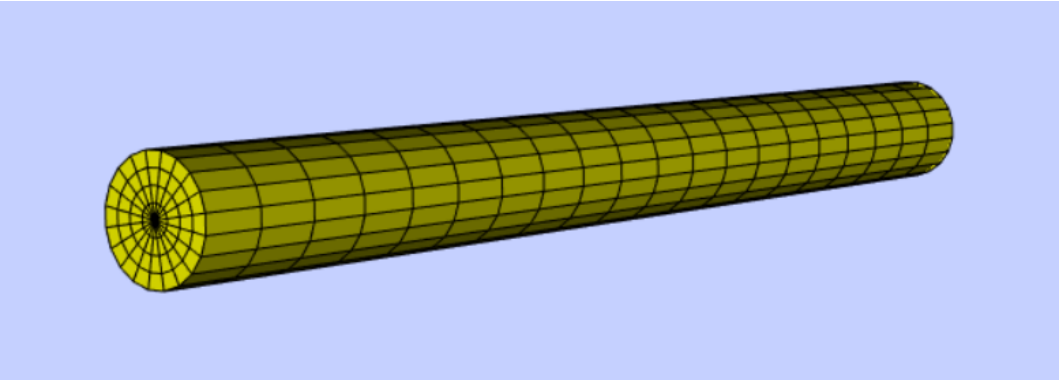

Figure 3.1: Example mesh of submerged tube

Variable	Name	Value
Modal degrees of freedom	N	10
Tube thickness	t	$0.04\mathrm{r}_s$
System mass	M	$0.15\ \rho\pi r_s^2 L$
Tube material damping	B_{vis}	$17.8\ \mathrm{kPa}\cdot\mathrm{s}$
Tube material elasticity	K_{mat}	$900\ \mathrm{kPa/m}^2$
Internal fiber pretension	T_s	38 kN
Mooring line stiffness	K_m	51 kN/m
Viscous damping coefficient	B_R	$8\pi{\cdot}10^{-6}$
Water density	ρ	$1025\ \mathrm{kg/m}^3$
Water depth	d	-45 m

3.1.3 Meshing

Each design mesh is generated as a cylindrical tube with its center at $(0, 0, z_s)$ (Fig. 3.1). The shortest deep water incident wavelength studied at our deployment location is 16.4 m, so we used a conservative mesh characteristic length-wise size of 0.667 m following a mesh convergence test repeated for multiple designs with stratified sampling. This length is adequate compared to the recommended maximum characteristic length of one-eighth an incident wavelength given by the meshing guidelines in [88].

3.1.4 Creating Mode Shapes

To assess the bulging device's structural deformations, we can define N =10 custom degrees of freedom in a frequency domain boundary element method tool that correspond to the device's deformation modes. This is known as generalized body modes analysis, and has been used to study structural deflections in both relatively rigid and flexible wave energy converters [89, 90]. We follow here the mathematical procedure of [91], who derived the modal equations of motion for the device, and the notation and modal matrices of [85].

We first define the variable $\chi(x,t)$ such that $\partial\chi/\partial t = U(x,t)$, the internal fluid velocity of inside of the enclosed tube. Using mass conservation and the assumption of small radial deformation amplitudes, we can use a Taylor series approximation to define the axisymmetric radial deformation δr of any point along the tube due to each mode:

$$\delta r = r(x,t) - r_s \tag{3.1}$$

$$\delta r = r_s\sqrt{1 - \frac{\partial\chi}{\partial x}} - r_s \tag{3.2}$$

$$\delta r \approx -\frac{r_s}{2}\frac{\partial\chi}{\partial x} \tag{3.3}$$

To define $\chi(x,t)$ for each set of design variables, we first need to solve the nonlinear dispersion relationships $f_1(\omega)$ and $f_2(\omega)$ for each modal frequency ω_n:

$$f_1(\omega) = 0 = \frac{k_{n,1}L}{2}\tanh\left(\frac{K_{n,1}L}{2}\right) - \frac{K_{n,1}L}{2}\tan\left(\frac{k_{n,1}L}{2}\right) \tag{3.4}$$

$$\begin{aligned} f_2(\omega) = 0 = {} & \frac{K_{n,2}L}{2}\tanh\left(\frac{K_{n,2}L}{2}\right) + \frac{k_{n,2}L}{2}\tan\left(\frac{k_{n,2}L}{2}\right) \\ & - \frac{\rho\pi r_s^2 L\cdot\omega_{n,2}^2}{-M\omega_{n,2}^2 + 2K_m}\left(\frac{K_{n,2}}{k_{n,2}} + \frac{k_{n,2}}{K_{n,2}}\right)\cdot\tanh\left(\frac{K_{n,2}L}{2}\right)\tan\left(\frac{k_{n,2}L}{2}\right) \end{aligned} \tag{3.5}$$

Where the modal wavenumbers $k_{n,i}$ and $K_{n,i}$ for each of the two mode types ($i = 1, 2$)

are related to each set of frequency roots $\omega_{n,1}$ and $\omega_{n,2}$:

$$k_{n,i}^2 = \frac{2\pi}{DT_s}\left(\sqrt{1+\frac{1}{\pi}T_s\rho D^2\cdot\omega_{n,i}^2}-1\right) \tag{3.6}$$

$$K_{n,i}^2 = \frac{2\pi}{DT_s}\left(\sqrt{1+\frac{1}{\pi}T_s\rho D^2\cdot\omega_{n,i}^2}+1\right) \tag{3.7}$$

And D is the distensibility, a geometry dependent stiffness parameter, of the tube material found by:

$$D = \frac{1}{\pi r_s t K_{mat}}$$

Where the tube thickness t and tube material elasticity K_{mat} are given in Section 3.1.2.

Initial tests from viewing plots of the dispersion function for multiple designs showed that modal frequencies were regularly spaced out by at least 0.1 to 0.3 rad/s from one another (Fig. 3.2), along with [85]'s results, so each set of nonlinear equations was solved by first discretizing a set of modal frequencies from a small value ϵ=10^{-4} to 10π rad/s by a conservative $\Delta\omega \approx$0.0005 rad/s. An approximation of each root was found by checking where the small change in frequency $\Delta\omega$ caused a change in sign of $f_1(\omega)$ or $f_2(\omega)$. Each of these frequencies was then used as a starting point for SciPy's [92] fsolve function to numerically find each actual root ω_n.

The frequencies were then sorted by magnitude from smallest to largest, and then trimmed off after n degrees of freedom. The two different mode shapes are then as follows:

$$\chi_{n,1} = c_1\sin\left(k_{n,1}x\right) - c_2\sinh\left(K_{n,1}x\right) \tag{3.8}$$

$$\chi_{n,2} = c_3\cos\left(k_{n,2}x\right) + c_4\cosh\left(K_{n,2}x\right) \tag{3.9}$$

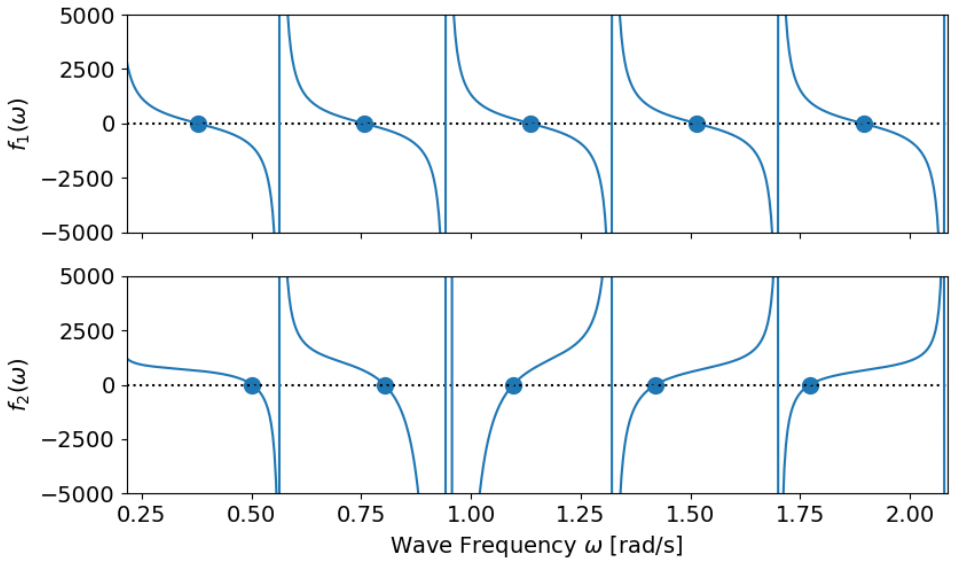

Figure 3.2: The dispersion relationship for a 1.10 m radius and 192.0 m long tube. Found roots are shown with dots. Note that extra error checking is required to not include $\omega \approx 0.94$ rad/s as a potential root of $f_2(\omega)$. This extra error checking was missed for the results included in this thesis, meaning that one potential modal degree of freedom is incorrect. However, final optimal design concept results are expected to be similar due to how much power is distributed in each concept's modes.

Where the constants c_1 to c_4 are as follows:

$$c_1 = \tanh\left(\frac{K_{n,1}L}{2}\right) \Big/ \cos\left(\frac{k_{n,1}L}{2}\right) \tag{3.10}$$

$$c_2 = \tan\left(\frac{k_{n,1}L}{2}\right) \Big/ \cosh\left(\frac{K_{n,1}L}{2}\right) \tag{3.11}$$

$$c_3 = K_{n,2}\tanh\left(\frac{K_{n,2}L}{2}\right) \Big/ \cos\left(\frac{k_{n,2}L}{2}\right) \tag{3.12}$$

$$c_4 = k_{n,2}\tan\left(\frac{k_{n,2}L}{2}\right) \Big/ \cosh\left(\frac{K_{n,2}L}{2}\right) \tag{3.13}$$

It should be noted that the hyperbolic factors $\cosh(K_{n,i}x)$ and $\sinh(K_{n,i}x)$ actually cause an overflow error for large values of $K_{n,i}x$, so we have to use the exponential limit of each mode shape function $\chi_{n,1}$ and $\chi_{n,2}$ to avoid overflow. For large combinations of modal wavenumbers $K_{n,i}$ and tube lengths L, the hyperbolic trigonometric terms $\cosh(K_{n,i}x)$ and $\sinh(K_{n,i}x)$ can cause an overflow error when using Python's built-in math library. To address this, we must catch the error when generating each mode shape and take the following limits for large positive x:

$$\sinh(K_{n,i}x) \approx \frac{\exp(K_{n,i}x)}{2} \tag{3.14}$$

$$\cosh(K_{n,i}x) \approx \frac{\exp(K_{n,i}x)}{2} \tag{3.15}$$

And large negative x:

$$\sinh(K_{n_i}x) \approx -\frac{\exp(-K_{n,i}x)}{2} \tag{3.16}$$

$$\cosh(K_{n_i}x) \approx \frac{\exp(-K_{n,i}x)}{2} \tag{3.17}$$

The two different mode shapes are then as follows for positive x:

$$\chi_{n,1} = c_1\sin(k_{n,1}x) - c_2\exp\left(K_{n,1}\left(x - \frac{L}{2}\right)\right) \tag{3.18}$$

$$\chi_{n,2} = c_3\cos(k_{n,2}x) + c_4\exp\left(K_{n,2}\left(x - \frac{L}{2}\right)\right) \tag{3.19}$$

And negative x:

$$\chi_{n,1} = c_1 \sin\left(k_{n,1}x\right) + c_2 \exp\left(K_{n,1}\left(-x - \frac{L}{2}\right)\right) \tag{3.20}$$

$$\chi_{n,2} = c_3 \cos\left(k_{n,2}x\right) + c_4 \exp\left(K_{n,2}\left(-x - \frac{L}{2}\right)\right) \tag{3.21}$$

Where the constants c_1 to c_4 are redefined as follows:

$$c_1 = \tanh\left(\frac{K_{n,1}L}{2}\right) \Big/ \cos\left(\frac{k_{n,1}L}{2}\right) \tag{3.22}$$

$$c_2 = \tan\left(\frac{k_{n,1}L}{2}\right) \tag{3.23}$$

$$c_3 = K_{n,2} \tanh\left(\frac{K_{n,2}L}{2}\right) \Big/ \cos\left(\frac{k_{n,2}L}{2}\right) \tag{3.24}$$

$$c_4 = k_{n,2} \tan\left(\frac{k_{n,2}L}{2}\right) \tag{3.25}$$

We then normalize each shape function χ_i according to [85] using scipy's integration library:

$$N_i^2 = \frac{1}{L}\int_{-L/2}^{L/2} \chi_i^2 dx + \frac{M}{\rho\pi r_s^2 L}\left(\chi_i\Big|_{L/2}\right)^2 \tag{3.26}$$

Where M is the dry total system mass we assume to be 15% of the internal fluid mass $m = \rho\pi r_s^2 L$. Normalization is necessary to ensure that each modal mass is the same value m when we later compute each modal response amplitude.

Mathematically, each function χ_i and derivative are redefined using the normalization factors as follows:

$$\chi_i := \frac{1}{N_i}\chi_i \tag{3.27}$$

$$\frac{\partial \chi_i}{\partial x} := \frac{1}{N_i}\frac{\partial \chi_i}{\partial x} \tag{3.28}$$

An example of the normalized shape functions for a given tube design are shown in Fig. 3.3

We then define the radial deformation function δr for each modal frequency according to (3.3), and include them as generalized degrees of freedom in our boundary element

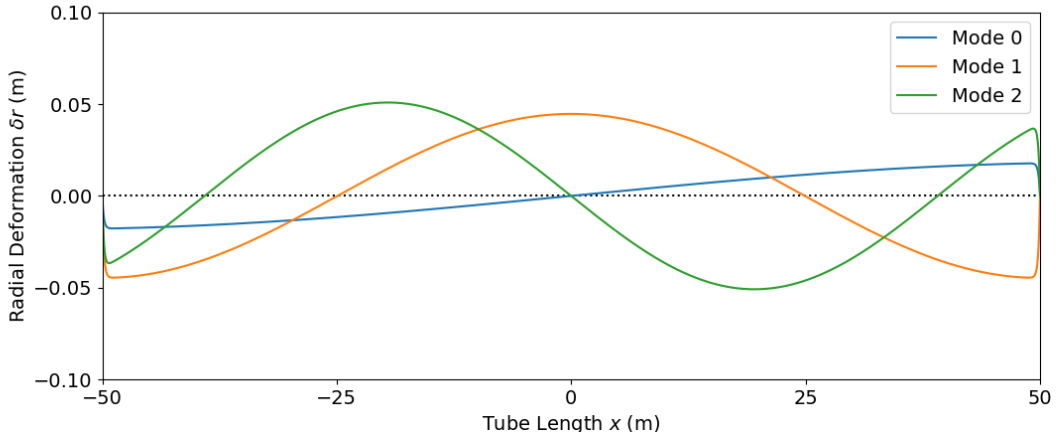

Figure 3.3: Natural modal deformation shape functions for a 100.0 m long tube with a 1.00 m radius. Maximum radial displacements for a unit response amplitude are approximately 2-5% of this radius for lower frequency modes, and are higher for higher frequency modes. Modes are listed numerically in order of increasing frequency.

method software Capytaine. Using the notation of [36], each mesh face centered at location (x_m, y_m, z_m) will have corresponding Cartesian deformations (u, v, w):

$$u = 0 \tag{3.29}$$

$$v = \frac{y_m}{r_s} \cdot \delta r \tag{3.30}$$

$$w = \frac{z_m - z_s}{r_s} \cdot \delta r \tag{3.31}$$

3.1.5 Assessing Modal Response Amplitudes

We then evaluate the added mass $\boldsymbol{A}(\omega)$, radiation damping $\boldsymbol{B}_{rad}(\omega)$, and excitation force $\hat{\boldsymbol{F}}_{ex}(\omega)$ matrices due to the waves radiated by each degree of freedom and diffracted by the still tube in a 0 degree incident wave. The notation $f(\omega)$ here denotes a function f of incident wave frequency ω. All hydrodynamic parameters were found in the boundary element method software Capytaine [32], a Python rewrite of the Matlab code Nemoh [33].

The frequency domain equation of motion for each modal degree of freedom k is as

follows:

$$\left(-\omega^2(\boldsymbol{M}+\boldsymbol{A}(\omega))+i\omega(\boldsymbol{B}+\boldsymbol{B}_{rad}(\omega))+\boldsymbol{C}\right)\begin{pmatrix}\hat{a}_1\\ \vdots\\ \hat{a}_n\end{pmatrix}=\hat{\boldsymbol{F}}_{ex}(\omega) \tag{3.32}$$

Where $\boldsymbol{M}$, $\boldsymbol{B}$, and $\boldsymbol{C}$ are the frequency independent contributions to the modal mass, damping, and stiffness matrices, respectively evaluated as:

$$\boldsymbol{M}=\rho\pi r_s^2 L\cdot\boldsymbol{I}_n \tag{3.33}$$

$$\boldsymbol{B}=\rho\pi r_s^2\eta\boldsymbol{\xi}+\rho B_R\boldsymbol{\epsilon} \tag{3.34}$$

$$\boldsymbol{C}=\begin{bmatrix}\omega_1^2 & & \\ & \ddots & \\ & & \omega_n^2\end{bmatrix}\boldsymbol{M} \tag{3.35}$$

$\boldsymbol{I}_n$ is an n x n identity matrix, and the modal damping terms $\boldsymbol{\xi}$ and $\boldsymbol{\epsilon}$ are due to wall damping and damping due to the tube's inner flow:

$$\boldsymbol{\xi}_{ij}=\int_{-L/2}^{L/2}\frac{\partial\chi_i}{\partial x}\frac{\partial\chi_j}{\partial x}dx \tag{3.36}$$

$$\boldsymbol{\epsilon}_{ij}=\int_{-L/2}^{L/2}\chi_i\chi_j dx \tag{3.37}$$

The constant η is a dissipation coefficient proportional to the material's total material damping B_{mat} and power take off damping B_{PTO} and related to the tube's thickness t and static radius r_s:

$$\eta=\frac{t\pi r_s}{\rho}(B_{mat}+B_{PTO}) \tag{3.38}$$

Where the total material damping B_{mat} is a function of the tube geometry and the constant B_{vis} power dissipation:

$$B_{mat}=\frac{1}{2\pi r_s^2}B_{vis} \tag{3.39}$$

And the power take off damping coefficient relates the radial deformation rate and

the stress in the power take off, as in [91]:

$$\sigma_{PTO} = B_{PTO}\left(2\pi r_s \frac{\partial r}{\partial t}\right) \tag{3.40}$$

Note that $\boldsymbol{\xi}_{ij}$ has the following alternative form that relates to the linearized tube deformations δr:

$$\boldsymbol{\xi}_{ij} = \frac{4}{r_s^2}\int_{-L/2}^{L/2}\left(-\frac{r_s}{2}\frac{\partial \chi_i}{\partial x}\right)\left(-\frac{r_s}{2}\frac{\partial \chi_j}{\partial x}\right)dx \tag{3.41}$$

$$\boldsymbol{\xi}_{ij} = \frac{4}{r_s^2}\int_{-L/2}^{L/2}\delta r_i \delta r_j dx \tag{3.42}$$

We then calculate the total dissipated power spectrum $P_{total}(\omega)$ due to each modal response amplitude velocity $\omega\hat{a}_k$:

$$P_{total}(\omega) = C_s \cdot \frac{1}{2}\rho\pi r_s^2 \eta\omega^2 \sum_m^n \sum_l^n \mathbb{R}(\hat{a}_m \hat{a}_l^*)\boldsymbol{\xi}_{ml} \tag{3.43}$$

The factor C_s is the proportion of tube circumference C_s below the free surface, we assume that only the submerged circumference of a neutrally buoyant device is able to deflect and harness power due to incoming waves. Where the multiplying constant C_s is given by the continuous function:

$$C_s = \begin{cases} 1 & z_s \leq -r_s \\ \left(\pi - 2\arcsin\left(z_s/r_s\right)\right)/\left(2\pi\right) & -r_s < z_s \leq r_s \end{cases} \tag{3.44}$$

A plot of the submerged power factor C_s as a function of the follows in Fig. 3.4.

This power spectrum is a useful metric for using the device as a passive or active floating breakwater. We are only interested here, however, in the mechanical power dissipated by the PTO $P_{PTO}(\omega)$ damping for potential conversion into electrical power, so we take a ratio of the PTO damping to the total material damping:

$$P_{PTO}(\omega) = \frac{B_{PTO}}{B_{PTO} + B_{mat}} P_{total}(\omega) \tag{3.45}$$

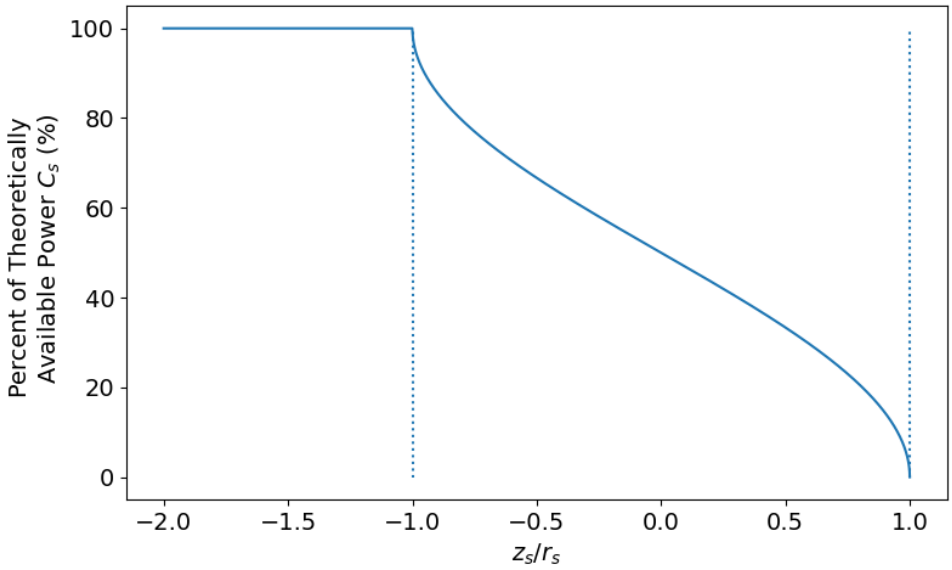

Figure 3.4: A percentage of available power for the submerged device as a ratio of its submergence z_s to static radius r_s. The left and right dotted lines respectively correspond to entirely submerged and floating tube designs.

3.1.6 Calculating the Objective Function

To simplify our analysis, we then use a probability distribution of our potential deployment location's annual wave frequencies to calculate the device's average power output μ_P due to solely changes in environmental wave frequencies:

$$\mu_P = \int_0^\infty P_{PTO}(\omega) \cdot p(\omega) d\omega \tag{3.46}$$

We chose to study the design parameters of an optimal design located at Humboldt Bay, CA, with our annual average wave period spectrum data divided into 82 equal period width bins from 3.2409 s to 17.8155 s (0.3527 to 1.9387 rad/s). We turned this into a frequency function from 0.3 to 2.0 rad/s that is linearly interpolated into 50 equally spaced incident frequencies (Appendix A.4). [93] $p(\omega)$ shown in Fig. 3.5:

We interpolated this probability distribution function when running frequency convergence tests, and normalizing the function by forcing the total probability of m frequencies

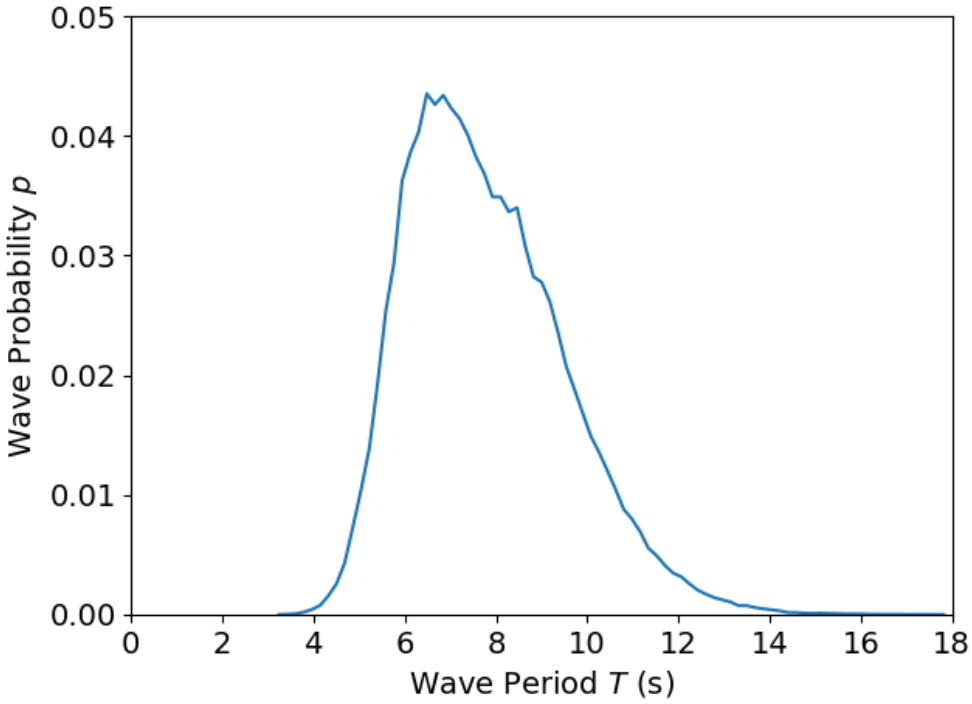

Figure 3.5: Probability distribution of incident wave periods at Humboldt Bay, California

to be 1. That is,

$$p(\omega) := \frac{p_k(\omega}{\sum_k^m p_k(\omega)} \tag{3.47}$$

The device power was found in every wave period at this location using a regular wave height of 1.0 m and weighted according to its probability of occurrence, similarly to the methodology presented in [94] and the correct order of magnitude as mentioned in [85].

Our final optimization problem is then as follows:

$$\begin{aligned} \text{minimize} \quad & f_{obj} = -\mu_P \\ \text{subject to} \quad & z_s \leq r_s \end{aligned}$$

The constraint that $z_s \leq r_s$ is a purely physical one - it means that the device must be partially submerged and not entirely above the free surface. Instead of enforcing this constraint explicity in our optimization or applying a mathematical penalty to our objective function evaluation, we evaluate a design that breaks this constraint to have exactly zero power (that is, $f_{obj} = 0$).

We also do not impose a constraint on the maximum deflection of the tube, so the uniform wave height can be chosen arbitrarily for direct search optimization purposes as long as it has a small amplitude. This is because direct search algorithms seek and move toward any found design improvements, and the uniform wave height only serves to vertically stretch the objective function. See Appendix A.1 for more details.

3.1.7 Finding the Optimal PTO Damping

After evaluating the hydrodynamic coefficients for a design, we optimize the value B_{PTO} using a one dimensional line search with the golden section method in scipy. The hydrodynamic properties of each mesh and modal degrees of freedom are both independent of the PTO damping, so the damping value can be tuned to each design to optimize the tube's total dissipated power. Tuning the damping value physically represents changing the voltage of the electroactive material [10]. We do this by iteratively solving Equations (3.32)-(3.46) for each tested value B_{PTO}, and searching for the maximum value of μ_P. μ_P is a convex function of B_{PTO} and has a single maximum value, as seen in Fig. 4.4. The influence of the optimal PTO damping value for a given tube design can be seen in

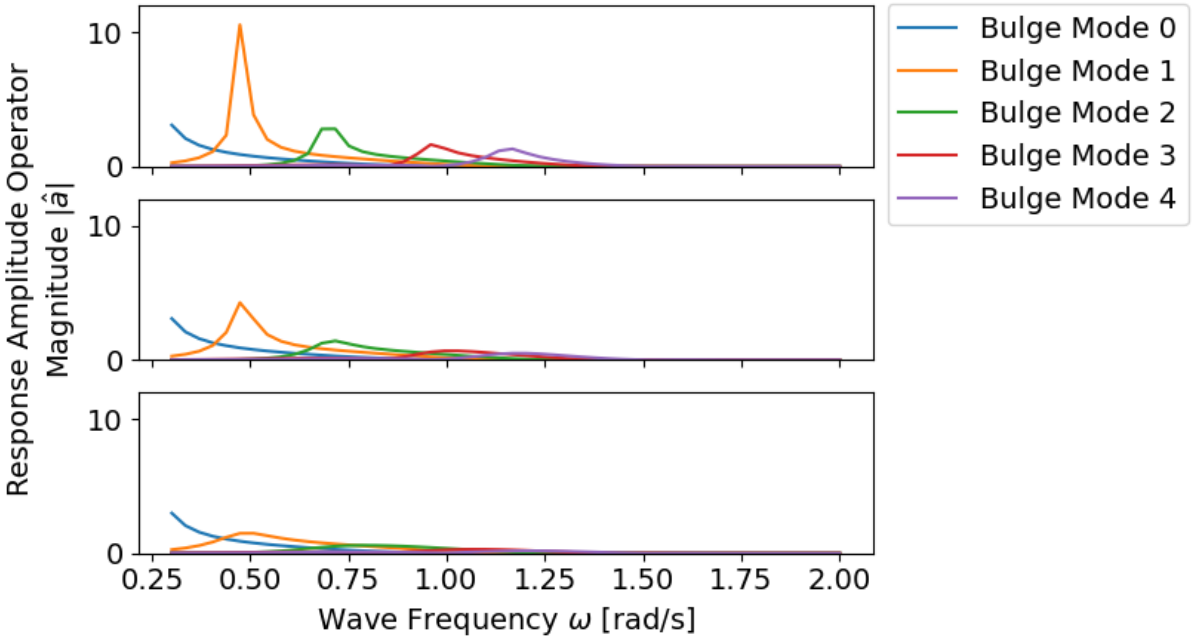

Figure 3.6: From top to bottom, the modal response amplitude operator magnitudes corresponding to one-third, one, and three times, the optimal value of B_{PTO} for mean power production purposes. Damping under the optimal value (top) leads to higher motion amplitudes with smaller material stresses for power production, and damping over the optimal value (bottom) leads to higher material stresses but lower motion amplitudes.

Fig 3.6, which shows the response amplitude operators for the first 5 modes of a tube design. Note that the optimal damping value was found for 10 modes, however.

3.2 Convergence Tests

3.2.1 Design Sampling

Convergence studies are necessary to ensure that the results of a design analysis are accurate for a given set of simulation conditions. While necessary for analyzing single designs, they are particularly relevant for design optimization studies which may be evaluating a wide range of potential design parameters. We used a uniform stratified

sampling method [86] to pick designs for several necessary convergence studies. This method divides up the space between the lower and upper bounds of each design variable, as given in Table 3.1.1, into equally spaced regions. The method ensures that each region for each variable is covered by exactly one design sample. We then randomly chose a point in each region, and then rounded each geometry and submergence design variable to the nearest discrete value. The three chosen designs from this sampling method are given in the table below. We also created a fourth design to be tested alongside the three sampled designs, that of a barely submerged tube ($z_s = -1.14 \cdot r_s$). We chose this fourth design in particular due to known numerical issues of similar designs near the free surface [48, 85].

Design	Radius	Length	Submergence	Mesh Cell Count
1	0.65	90.0	-11.25	2360
2	1.10	192.0	-4.00	5000
3	2.75	22.0	-1.50	874
4	1.10	35.0	-1.25	1060

It should be noted that the randomly generated submergence for the third design was initially 2.75 m, which would have produced a zero power device due to floating entirely above the water surface. This value was then manually adjusted in the chosen region to provide a more physically meaningful convergence test for an approximately half submerged device.

3.2.2 Convergence Study: Mode Count

We performed a mode count convergence study first, where each device was first simulated starting with 1 modal degree of freedom. We then incremented the total number of simulated modal degrees of freedom by 1 until the final estimated power value μ_P had leveled out.

Each mode count study was performed on a conservatively sized mesh with a characteristic length of 0.8 m, an end cap characteristic radial length of 0.2 m, and 20 angular divisions along the tube's outside. Each simulation was also completed on a conservative amount of 80 equally spaced wave frequencies from 0.3 rad/s to 2.0 rad/s.

We chose the final stabilized value at 12 modes as a reference point for each design,

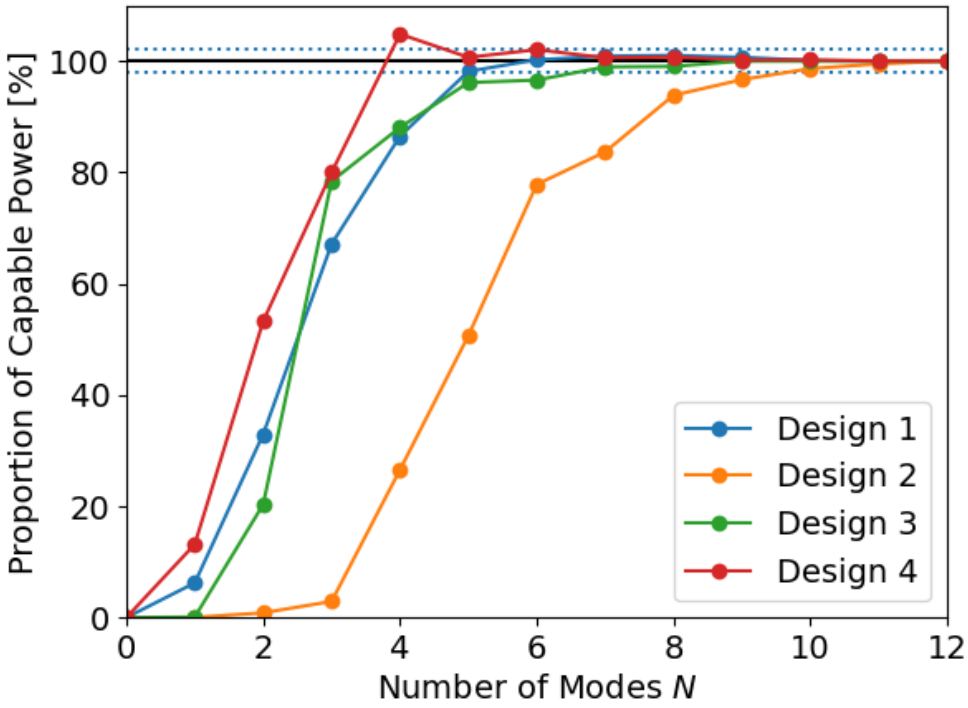

Figure 3.7: Each additional modeled degree of freedom contributes an additional amount of power, but this effect levels out to a negligible amount after about 10 modes, as it has the highest number of natural frequencies with the range of incident frequencies.

and found that anywhere from 5 to 10 modes were necessary to be within 2% of this value (Figures 3.7 and 3.8). We then chose the highest of 10 modes too simulate for each tested design in the design automation and optimization process.

3.2.3 Convergence Study: Mesh Cell Size

Next we performed a mesh convergence study for the four designs (Figure 3.9). Each mesh was refined using the same set of spacings of characteristic lengths, end cap radial lengths, and angular divisions. Each simulation was also completed on a conservative amount of 80 equally spaced wave frequencies from 0.3 rad/s to 2.0 rad/s.

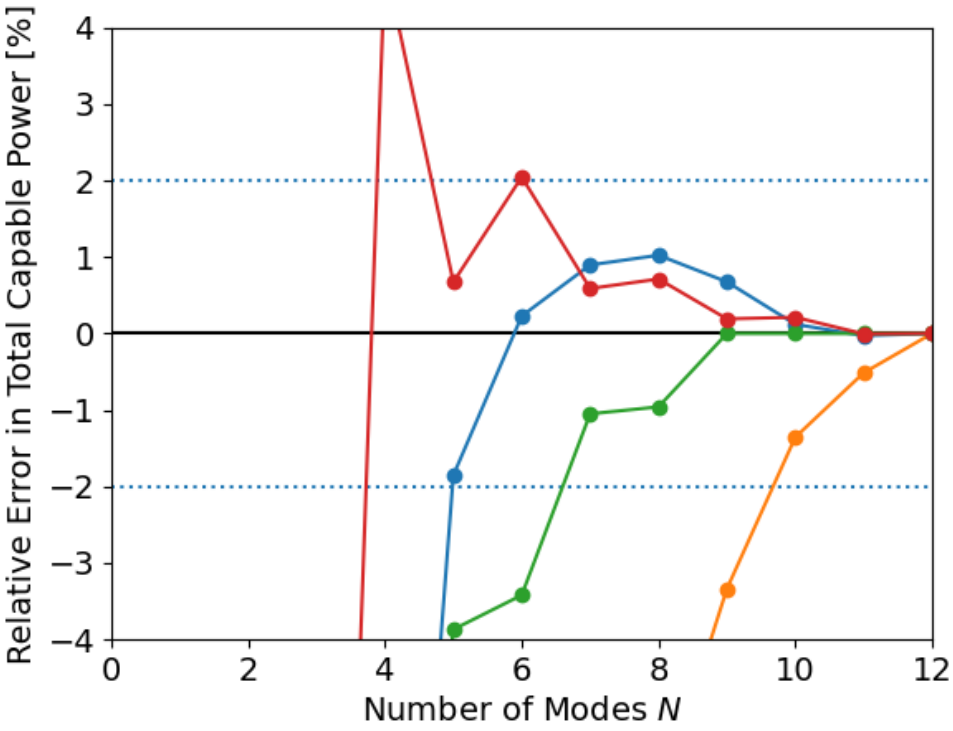

Figure 3.8: A zoom in of Figure 3.7, with a relabeled y-axis to show the relative percent error from the final stabilized power value. Anywhere from 5 to 10 modes were necessary to stay within 2% of the final power value. Note that Design 2, the longest device at 192.0 m, requires the most modes to converge.

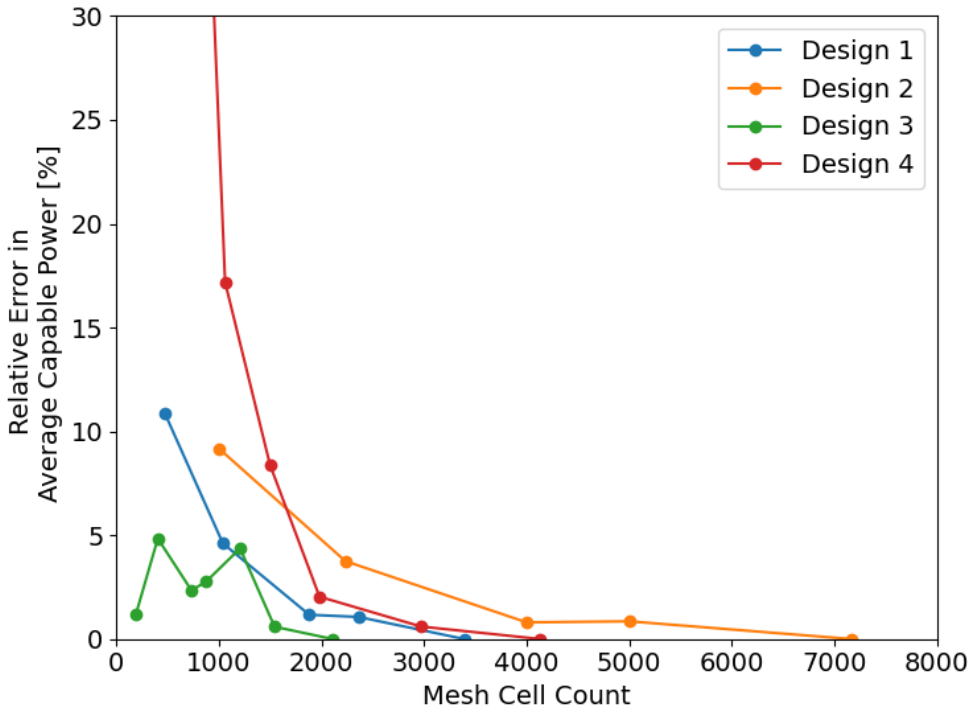

Figure 3.9: Each design mesh is considered to be converged when the slope of the line starts to become horizontal. Note that Design 4, the design submerged just under the free surface, has an error of up to 177% for its least resolved mesh, whereas each other mesh has under 15% error for their least resolved meshes.

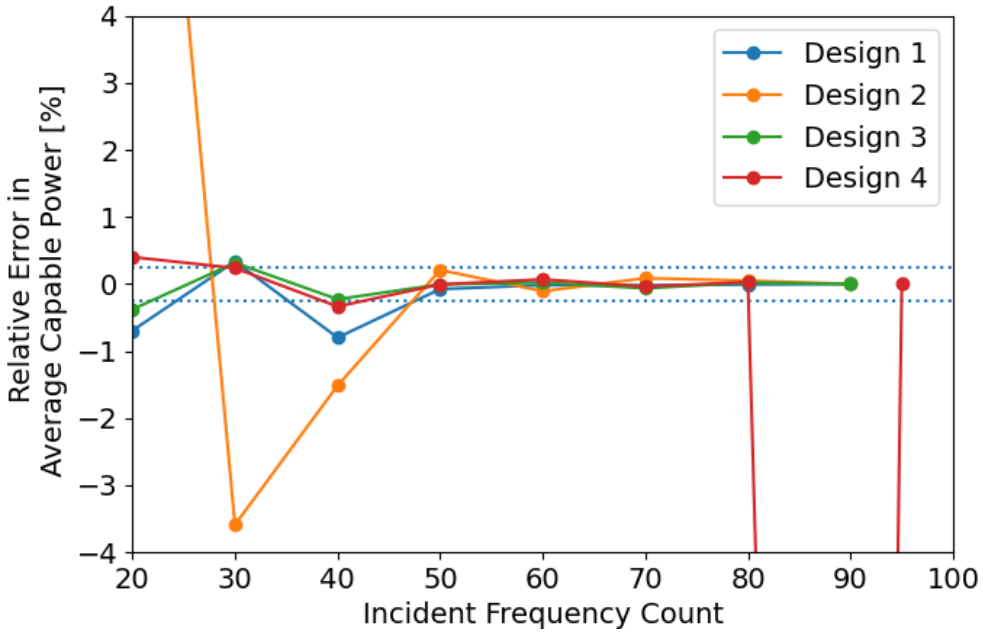

Figure 3.10: A subset of the frequency convergence study from 20 to 95 wave frequencies. We found that 50 equally spaced incidental wave frequencies were necessary for convergence. Each horizontal dotted line shows a 0.25% error from the final value at either 90 or 95 frequencies. Note the sharp dip in accuracy at 90 frequencies for Design 4, discussed in the next section.

3.2.4 Convergence Study: Incident Wave Frequencies

Our third and last convergence study was testing how many equally spaced incident wave frequencies we needed from 0.3 to 2.0 rad/s for our final power value to converge. The probability of each wave frequency was interpolated from the incident frequency distribution and normalized to a total probability of 1 (Eqn. (3.47)). We tested anywhere from 5 to 95 incident wave frequencies, and decided on 50 wave frequencies as the converged value (Fig. 3.10).

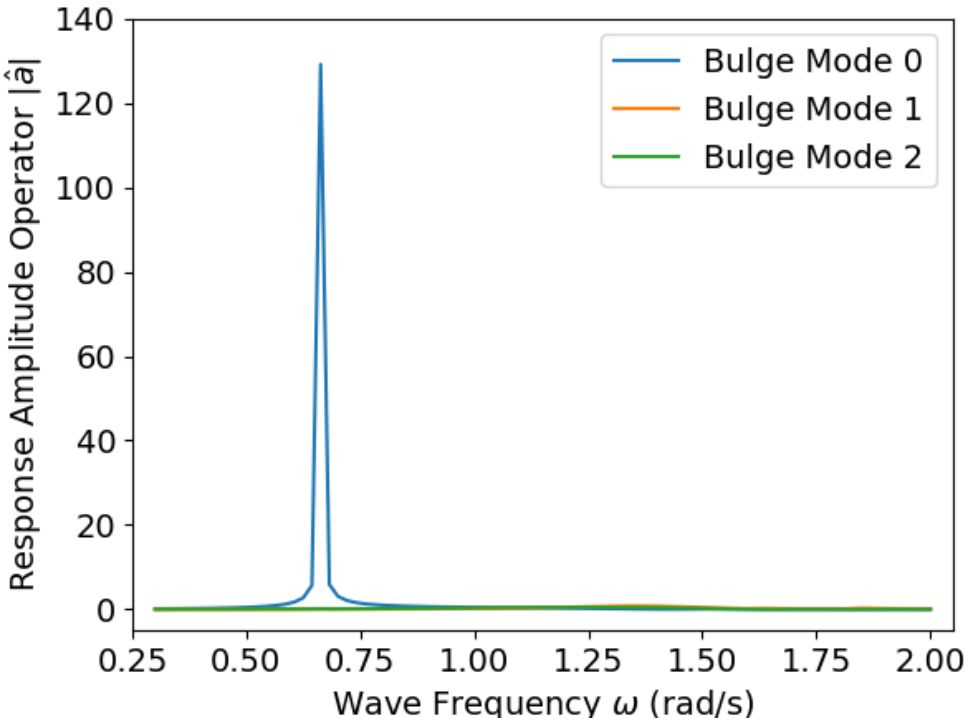

Figure 3.11: Concept simulation error can occur when a simulated incident wave frequency aligns too closely to a system modal frequency. In this case, the modal response amplitude forces a physically impossible displacement many times the total tube radius, which is exploited by the line search for the optimal tube damping.

3.2.5 Convergence Instabilities for Barely Submerged Tubes

One issue arose in particular when performing frequency convergence tests for a device near the free surface, Design 4 (Figs. 3.11 and 3.12). The error was due to a tube's 0th modal frequency ($\omega_{0,2} \approx 0.6639$ rad/s) corresponding very closely to a simulated wave frequency (0.6629) when simulating using 90 equally spaced wave frequencies for the design.

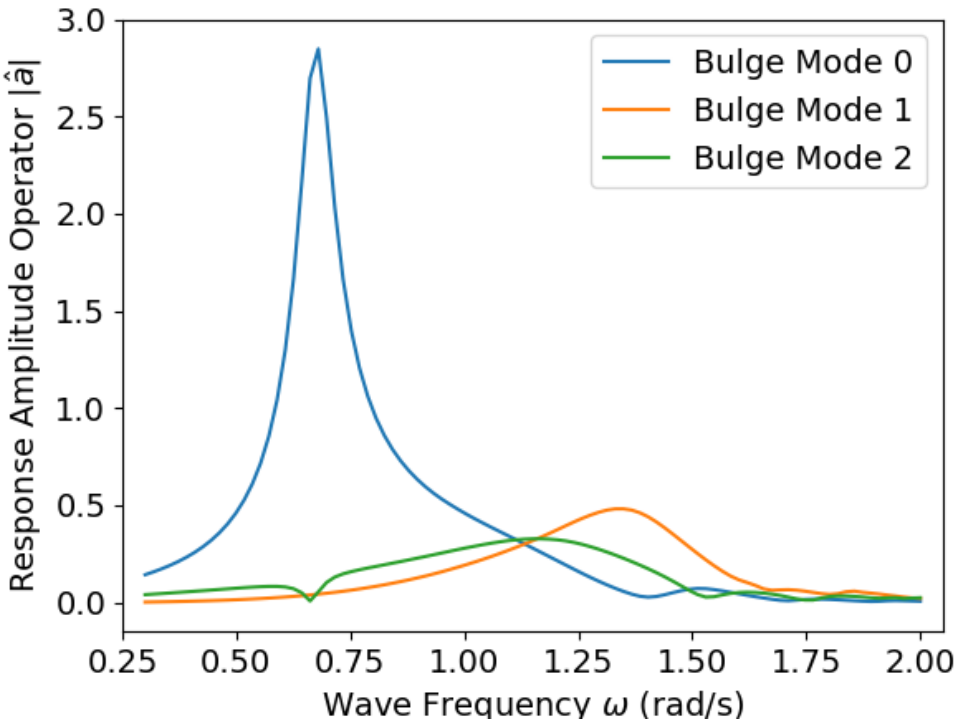

Figure 3.12: The simulation error seen in Fig. 3.11 is only fixed by simulating at a different number of incident wave frequencies. Automating this process was not performed here, although could be done by detecting when any simulated and modal frequencies align too closely and then changing the number of incident frequencies.

3.2.6 Update design

We then update the current design variables $\vec{x}_c$ depending on how well it evaluated relative to the last tested design $\vec{x}_{new}$. If the last used move $\alpha\vec{d}$ resulted in an improved move, we try it again until there is no more improvement. The entire function evaluation and design variable update process is listed in Algorithm 1, and can be seen as an extension of a greedy Hooke and Jeeves algorithm with the dynamic ordering of a generalized pattern search algorithm [86]. The algorithm can be considered greedy because it immediately chooses the first evaluated neighbor in design space that evaluates better than itself. Dynamic ordering works to shuffle the last successful move to the first next evaluated move for the next design. In this way, the number of steps is only decreased by a factor $\gamma = 1/2$ after all potential moves have been evaluated and found to be worse.

Algorithm 1 Discrete optimization algorithm for finding an optimal flexible tube design

Input

$\vec{x}_0$ Starting design variables
$\vec{d}_k$ Possible design change vectors
α_0 Starting step size

Output

$\vec{x}_{opt}$ Optimal design variables
f_{opt} Optimal objective function value for the optimization problem

1. Set the current design location $\vec{x}_c$ and objective function value f_c. This is equal to the starting design variables for the 1st iteration, and the best design found at any time during the optimization run.
2. Attempt a new move in design space $\vec{x}_{new} = \vec{x}_c + \alpha\vec{d}_k$ along the current search direction.
3. Check that the given design is within the given problem bounds, and reject the move if not.
4. Generate a mesh using the geometry design variables r_s, L, and z_s.
5. Calculate the design's modal frequencies ω_n using all of the design variables.
6. Create radial deformation modes using the modal frequencies, then convert each mode to Cartesian coordinates for each mesh face.
7. Evaluate the added mass, radiation damping, and excitation force matrices for each incident wave frequency using a boundary element method software.
8. Repeat steps a) to c) to optimize the damping value B_{PTO} for the design using a line search method.
   (a) Calculate the response amplitude $\hat{a}_n$ for each mode.
   (b) Calculate the dissipated power spectrum $P_{tot}(\omega)$.
   (c) Weight the power spectrum according to the wave environment to find the mean power value μ_P.
9. Find the next search direction to move, and check for convergence.
   (a) If $f_{new} < f_c$, keep the move to the new design $\vec{x}_{new}$ and set the current move to be first in the order of move directions. Keep α at the same value. Set $f_{opt} = f_{new}$, and go to 1).
   (b) If all variables have been searched without finding any better solution, reduce α by a factor of 1/2 and go to the first search direction $\vec{d}_k$. Go to 2).
   (c) If $\alpha = 1$ and there are no better moves along any search direction for any variable, the optimization is considered to be converged. Return $\vec{x}_{opt}$ and f_{opt}.

Chapter 4: Results & Discussion

4.0.1 Optimal Design Variables

We used a randomly generated discrete point as a starting point $\vec{x}_0$ for the direct search algorithm, with design variables as follows:

$$\vec{x}_0 = [r, L, z_s]$$
$$\vec{x}_0 = [2.5, 30.0, 2.25] \text{ m}$$

The algorithm converged to the final design in 51 iterations:

$$[r, L, z_s]_{opt,0} = [1.15, 200.0, -1.25] \text{ m}$$

With an objective function value of

$$f_{opt,0} = -654 \text{ kW}$$

The total computation time required to perform the entire design optimization was 69.8 hours. This indicates that instead of being designed to resonate at the solely one wavelength corresponding to the dominant wave frequency, an optimal tube's length should be simultaneously tuned to respond to multiple wave periods. In addition, it should be submerged just entirely below the water surface for maximum power dissipation.

4.0.2 Hydrodynamics of the Optimal Design

The first three mode shapes of this design can be seen in Fig. 4.1. Each mode shape has a maximum normalized radial deformation of about 0.05 to 0.15 m, or about 2 to 6% of the tube's radius. Multiplying the mode shape by its corresponding response amplitude magnitude $|\hat{a}|$ lets us find the maximum actual deformation along the tube at any given point and incident wave frequency due to a given mode (Fig. 4.3).

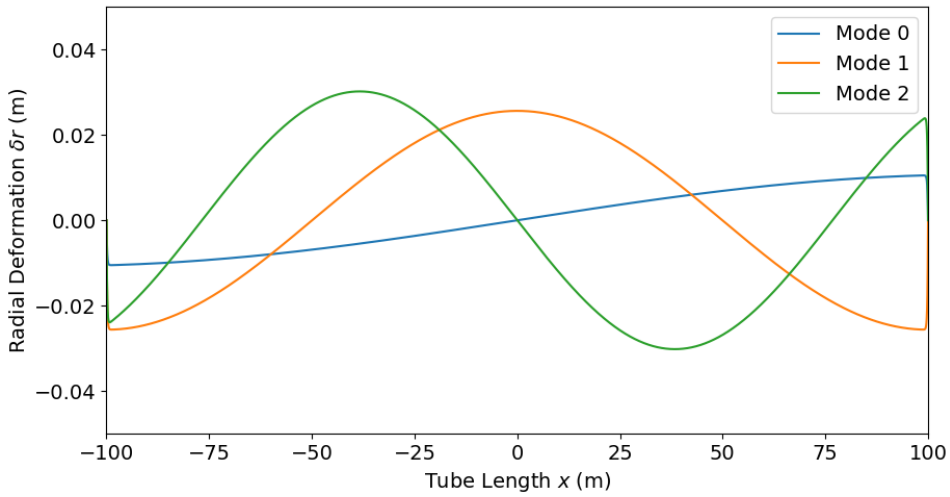

Figure 4.1: Radial deformation mode shapes of the optimal constrained design.

The added mass of the first 5 modes can be seen in Fig. 4.2.

We can see that the maximum response amplitude decreases for the higher frequency modes that have higher amplitudes, meaning that each of the three shown modes has approximately the same radial deformation as the others at their maximum response. The 0th mode appears to have the largest bandwidth overall, with the 1st and 2nd modes both having a sharper peak along the incident wave periods.

The dissipated power take off power spectrum $P_{PTO}(\omega)$ for the optimal constrained design can be seen in Fig. 4.4. The period weighted area under this curve gives us the mean dissipated power dissipated by the power take off material μ_P, as in (3.46). We see for the optimal design that it has a sharply decreasing power spectrum for frequencies about 1.15 rad/s, or below 5.5 second waves with approximately a 46.5 m wavelength.

The optimal power take off damping value for the optimal constrained design can be seen in Fig. 4.5. The curve is convex and has only one global optimum, showing that a line search is appropriate to solve for each design's optimum damping.

The impedance of the first three modes for the optimal design can be found in Fig. 4.6. We can see that the lowest mode has the lowest impedance across the incident wave frequencies, and monotonically increases with respect to each frequency. Higher

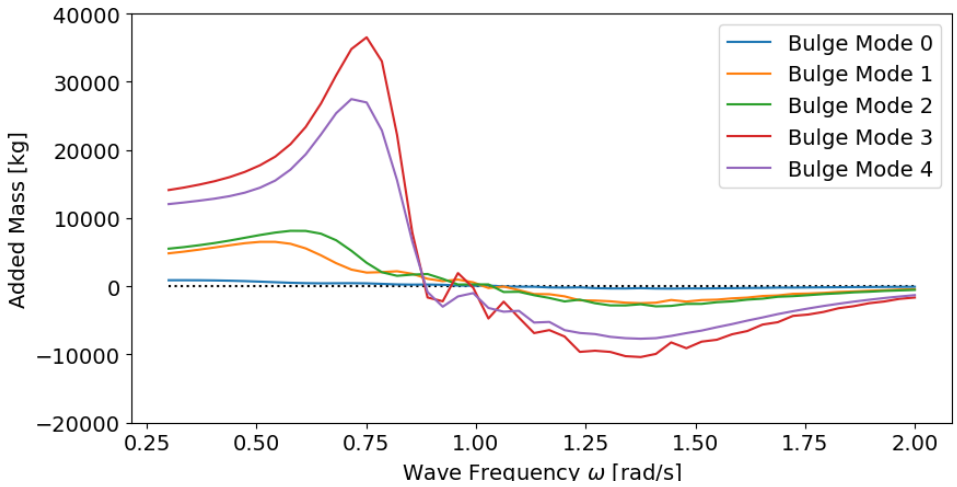

Figure 4.2: Added mass of the optimal design's first five natural modes. The dotted line is at 0 kg, showing that each mode has a negative added mass for certain frequency ranges. Device modes are sorted in order of increasing frequency.

frequency modes have consistently higher impedance values than their lower frequency counterparts.

4.0.3 Search Space Results

Our optimization algorithm's search history for the optimal tube length shows that it was able to successfully search a subset of the design space using a relatively small number of iterations. The search history of each design variable is considered in the captions of Figs. 4.7-4.9.

4.0.4 Validation Study with Bayesian Optimization

Because the direct search algorithm is inherently a local search, we decided to apply a Bayesian optimization algorithm as a validation measure to search for a globally optimal solution. Bayesian optimization works by initially sampling the function to be optimized, and creating a model of our objective function that can be subsequently sampled to make a more accurate model [95]. We connected the open source package Bayesian

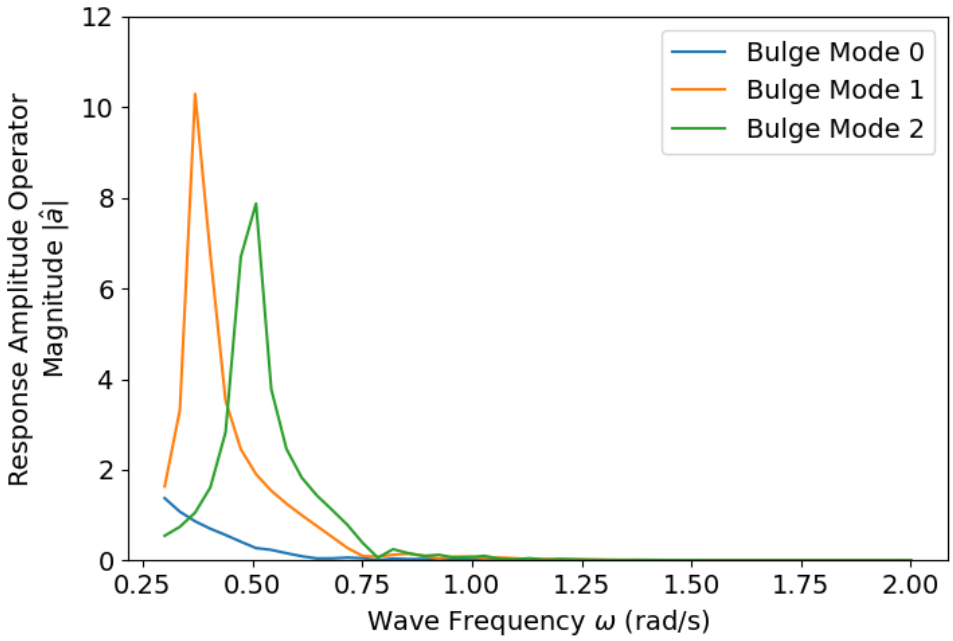

Figure 4.3: Response amplitude operators for all ten mode shapes of the optimal constrained design. Higher frequency modes generally move from left to right and show lower amplitudes at higher frequencies, but for mode shapes which generally have higher radial displacements.

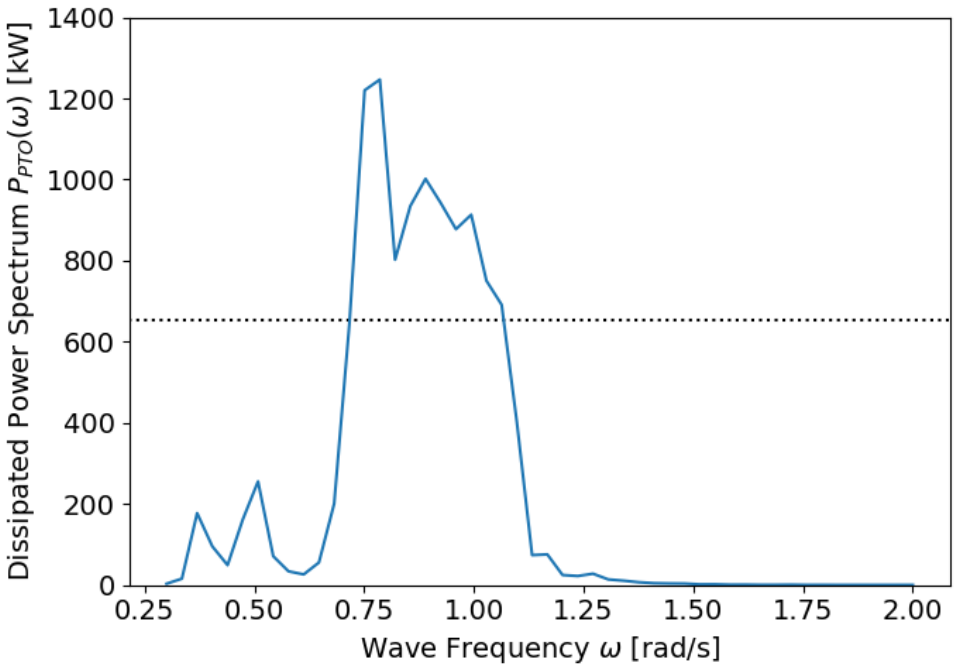

Figure 4.4: The dissipated power spectrum of the optimal device's Power Take Off. The dotted horizontal line shows the probability averaged mean dissipated power.

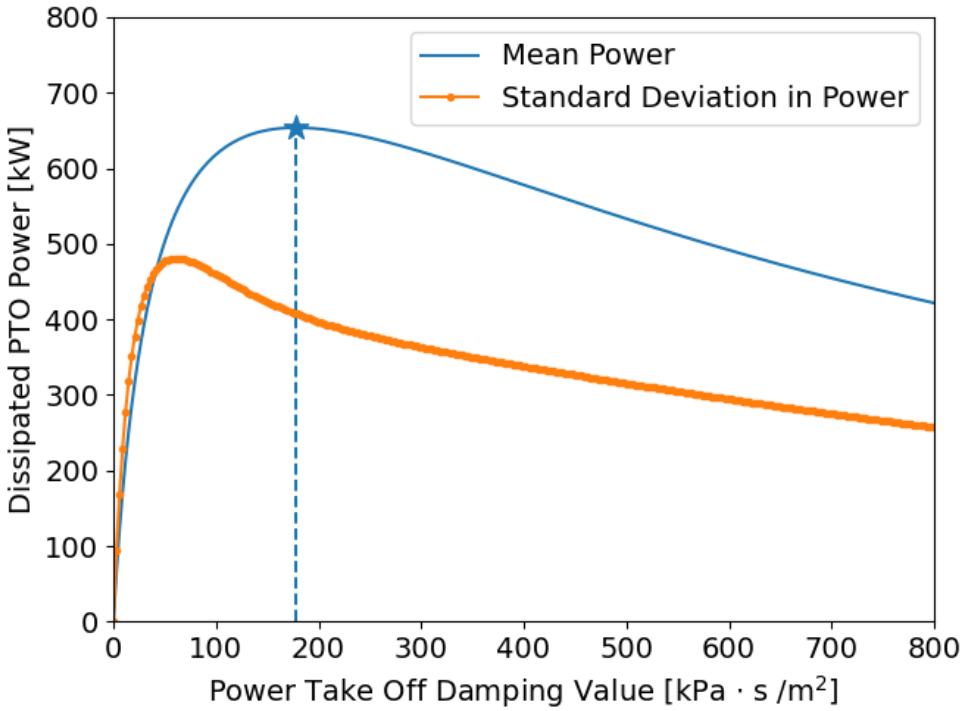

Figure 4.5: The relationship between the constant Power Take Off dissipation value and the mean and standard deviation of the tube's dissipated power spectrum. The single optimal value of B_{PTO} is shown with the dotted line and star.

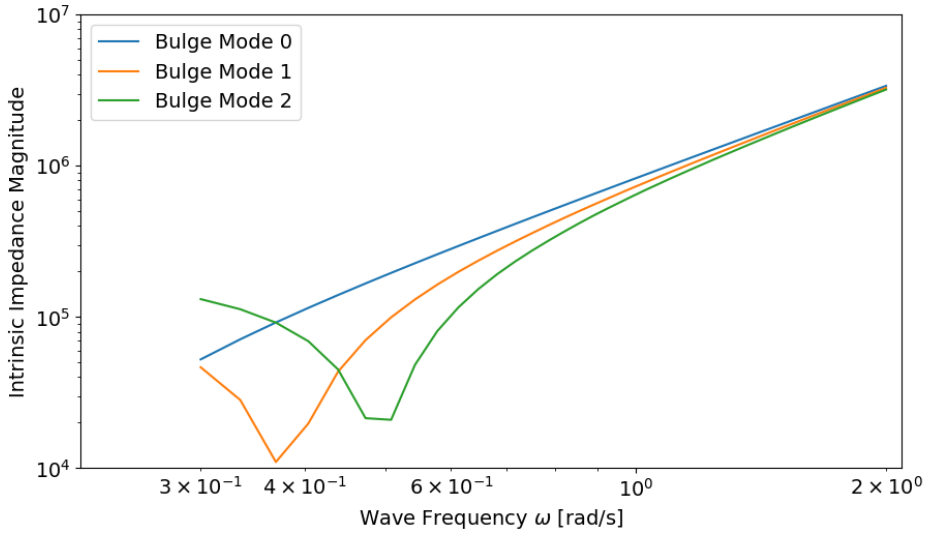

Figure 4.6: Impedance values for the optimally designed tube's three lowest frequency modes.

optimization package pyGPGO [96] to our design automation code, using a Gaussian process with a squared exponential kernel. We used a characteristic length-scale of 3 for the kernel with a zero valued noise variance due to our simulations being deterministic. We were interested as well in using the algorithm with a number of iterations on the order used for our Hooke and Jeeves algorithm. The acquisition function used to choose each next design point was based on the best expected improvement, and was found in the software using a multistart algorithm from 100 different points.

We ran two separate optimization runs: the first (labeled 1) with 20 initial samples and 40 additional points, and the second (labeled 2) with 40 initial samples and 60 additional points. The two best solutions found from each are as follows:

$$\vec{x}_{opt,1} = [r_s, L, z_s]_1 = [1.10, 197.57, -2.91] \text{ m}$$
$$\vec{x}_{opt,2} = [r_s, L, z_s]_2 = [1.76, 188.47, -1.92] \text{ m}$$

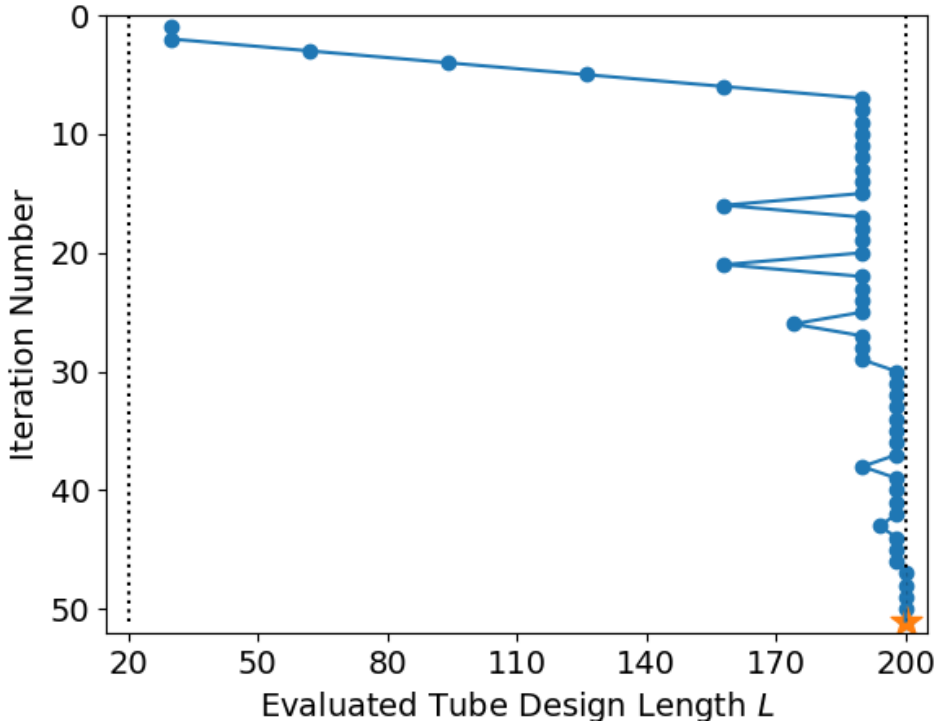

Figure 4.7: Search history for the optimal tube length over the course of our discrete algorithm. The optimization quickly moved towards longer designs and converges to a tube length of 200.0 m.

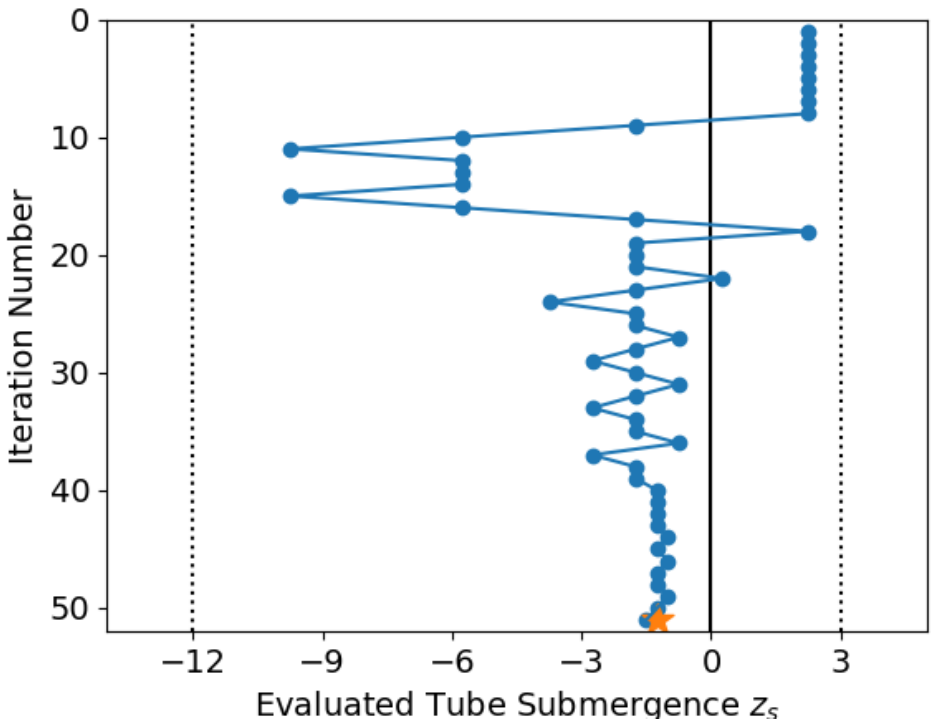

Figure 4.8: Search history for the optimal tube submergence over the course of our discrete algorithm, with a device at 50% submergence marked with a solid black line. The method is able to search both floating and deeper designs, converging to a final submergence of just below the free surface at -1.25 m.

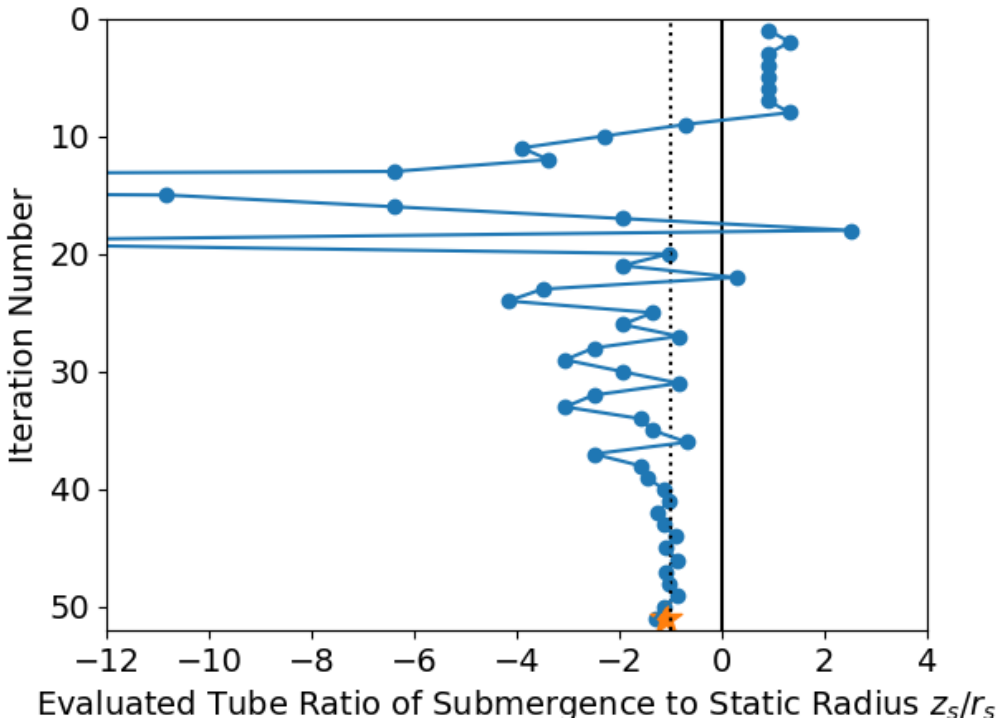

Figure 4.9: Search history for the optimal ratio of submergence to radius. Designs submerged entirely below the free surface (z_s/r_s=-1) are to the left of the black dotted line.

With respective objective function values of:

$$f_{opt,1} = -272 \text{ kW}$$
$$f_{opt,2} = -343 \text{ kW}$$

Both of these designs solutions found designs on a similar geometry scale as the best Hooke and Jeeves design but with worse (higher) objective function values. Each optimal geometry is close to the upper bound of design lengths too along with having a similar ratio of submergence to radius (1.09) as the original and the same order of magnitude in objective function value. An important consideration here is that these results were found using 10.6 and 23.6 hours of computational time, an amount significantly lower than the 69.8 hours required for the direct search algorithm. This is most likely because the direct search algorithm searched primarily tube designs with long lengths (Fig. 4.7), leading to longer evaluations times per iteration. On the other hand, the Bayesian optimization algorithm spends more time exploring the entire design space, leading to shorted evaluation times. We should note, however, that a different convergence criterion should be used other than an iteration count used here; we recommend adjusting the bounds of the problem based on the results here, to adjust the characteristic length-scale accordingly on the new bounds, and using a convergence criterion smaller that the expected improvement drop below a certain small value. Adjusting the bounds of the problem, however, will most certainly increase the required computational time required to convergence.

Chapter 5: Conclusions

Flexible wave energy converters are a potentially promising additional method of pursuing ocean energy power, but computational models to test even a single design are time and resource intensive, requiring as long as a few hours to evaluate just the linear dynamics of a single design. Because of this, finding the optimal geometry for a given wave environment within a practical amount of time requires as few function evaluations as possible. Different optimization methods than typically used in the wave energy converter design optimization field are then needed to find a different design.

We optimized the design of a submerged flexible wave energy converter by co-optimizing its submergence and geometry, aiming to improve the expected power output of the device. I specifically designed an opportunistic direct search algorithm inspired by a Hooke and Jeeves and extended pattern search algorithm but using a relatively coarse termination condition, effectively creating a discrete search space. I validated my final result using a more global Bayesian optimization algorithm, which produced a similar result but at the fraction of the total computational cost of the direct method. My work is also the first work that I know of to use the open source boundary element software Capytaine for wave energy converter design concept automation and optimization.

A simpler direct search optimization algorithm found an optimal design solution by exploiting designs that performed better, albeit at a higher computational cost around that optimal design. On the other hand, a Bayesian algorithm found a worse solution by a similar iteration requirement to the direct search, but at less than one sixth of the computational time.

My contributions to the research field include: using sampling techniques to ensure mesh, frequency, and mode convergence across a range of potential design options; applying design automation methods to automate modeling a flexible wave energy converter; allowing both floating and submerged designs to be tested; using a direct search design automation method to optimize an effectively discretized design space; and validation testing using a Bayesian optimization method.

As this work is on the forefront of a new area of research, it points to a more interesting

future for the optimization of both other flexible wave energy converter designs, as well as considering optimization algorithms of variable cost functions. We only considered the optimal geometry of a device that can be defined using relatively few design variables. Other design variables of interest would be linearized material and mooring parameters such the internal fiber pretension, tube thickness, material elasticity, and mooring line stiffness, as well as changing the system's mass. For higher numbers of design variables, it may be useful to directly use other surrogate modeling techniques such as response surface methods to approximate the mean power objective function. A response surface function could then be quickly optimized using a population based algorithm such as a particle swarm optimization or a genetic algorithm.

Additional work on this device in particular could benefit from incorporating additional rigid body degrees of freedom for a freely moving tube, as would incorporating device material nonlinearities. This would prove especially useful in a simulation software such as WEC-Sim that could directly incorporate the hydrodynamic coefficients found by Capytaine. Other objectives are important to search too - of particular interest for a flexible device are material failure considerations due to fracture or buckling. Directly incorporating reliability into calculating long-term wave loading would be important work to include in future studies as well, especially considering irregular sea states with high significant wave heights. Of interest in particular for the submerged tube is incorporating constraints on the total motion that are directly related to both the mode shapes and response amplitude operators. The difficulty of such work is treated more thoroughly in Ancellin et al. [85].

Other potential flexible wave energy design archetypes can be optimized, of course - of particular interest would be devices that not on the length scale of incoming waves, such as a flexible bottom mounted oscillating surge device.

Further work is needed here to directly incorporate a cost proxy to penalize increasing material or power take off design requirements, or by constraining the maximum radial deformation response in an irregular sea state instead of the uniform regular waves used here. More work could be done to study and optimize other flexible design archetypes that have different mode shapes to the submerged tube considered here.

The long function evaluation times required to simulate a single design in this study are an especially interesting use of design optimization algorithms, and more work is needed to determine tradeoffs between design improvements and the computational effort

needed to find them.

Bibliography

[1] BC Boren and J Weber, *Flexible wave energy converter*, U.S. Patent 0 054 820, Feb. 2021.

[2] J Pollack and PF Jean, *Wave energy converter*, U.S. Patent 0 019 498, Jan. 2010.

[3] A Kurniawan, JR Chaplin, DM Greaves, and M Hann, "Wave energy absorption by a floating air bag", Journal of Fluid Mechanics **812**, 294–320 (2017) 10.1017/jfm.2016.811.

[4] G Moretti, GP Rosati Papini, L Daniele, D Forehand, D Ingram, R Vertechy, and M Fontana, "Modelling and testing of a wave energy converter based on dielectric elastomer generators", Proceedings of the Royal Society of London Series A **475**, 20180566 (2019) 10.1098/rspa.2018.0566.

[5] JR Chaplin, V Heller, FJM Farley, GE Hearn, and RCT Rainey, "Laboratory testing the Anaconda", Philosophical Transactions of the Royal Society A: Mathematical, Physical and Engineering Sciences **370**, 403–424 (2012) 10.1098/rsta.2011.0256.

[6] M Blanco, M Lafoz, D Ramirez, G Navarro, J Torres, and L Garcia-Tabares, "Dimensioning of Point Absorbers for Wave Energy Conversion by Means of Differential Evolutionary Algorithms", IEEE Transactions on Sustainable Energy **10**, 1076–1085 (2019) 10.1109/TSTE.2018.2860462.

[7] H Mankle, Z Morrell, I Williams, G Bacelli, V Neary, B DuPont, and RG Coe, "Co-optimization of Sizing and Controls for a Point-Absorber Wave Energy Converter", 23.

[8] A McCabe, "Constrained optimization of the shape of a wave energy collector by genetic algorithm", Renewable Energy **51**, 274–284 (2013) 10.1016/j.renene.2012.09.054.

[9] A Garcia-Teruel and DIM Forehand, "Optimal wave energy converter geometry for different modes of motion", 8.

[10] P Jean, A Wattez, G Ardoise, C Melis, R Van Kessel, A Fourmon, E Barrabino, J Heemskerk, and JP Queau, "Standing wave tube electro active polymer wave energy converter", in Electroactive polymer actuators and devices (eapad) 2012, Vol. 8340, edited by Y Bar-Cohen, Society of Photo-Optical Instrumentation Engineers (SPIE) Conference Series (Apr. 2012), p. 83400C, 10.1117/12.934222.

[11] C Graf, J Maas, and D Schapeler, "Energy harvesting cycles based on electro active polymers", in SPIE Smart Structures and Materials + Nondestructive Evaluation and Health Monitoring, edited by Y Bar-Cohen (Mar. 2010), p. 764217, 10.1117/12.853597.

[12] WN Adger, JM Pulhin, J Barnett, GD Dabelko, GK Hovelsrud, M Levy, O Spring, CH Vogel, H Adams, J Hodbod, S Kent, M Tarazona, P Aldunce, and R Leichenko, *Climate Change 2014 Impacts, Adaptation, and Vulnerability, Part A: Global and Sectoral Aspects* (Intergovernmental Panel on Climate Change, 2014), p. 37.

[13] S Pacala, "Stabilization Wedges: Solving the Climate Problem for the Next 50 Years with Current Technologies", Science **305**, 968–972 (2004) 10.1126/science.1100103.

[14] M Lehmann, F Karimpour, CA Goudey, PT Jacobson, and MR Alam, "Ocean wave energy in the United States: Current status and future perspectives", Renewable and Sustainable Energy Reviews **74**, 1300–1313 (2017) 10.1016/j.rser.2016.11.101.

[15] "Powering the Blue Economy: Exploring Opportunities for Marine Renewable Energy in Maritime Markets", 207.

[16] G Chang, CA Jones, JD Roberts, and VS Neary, "A comprehensive evaluation of factors affecting the levelized cost of wave energy conversion projects", Renewable Energy **127**, 344–354 (2018) 10.1016/j.renene.2018.04.071.

[17] GM Paredes, L Bergdahl, J Palm, C Eskilsson, and FT Pinto, "Station keeping design for floating wave energy devices compared to floating offshore oil and gas platforms", 10.

[18] Mirko Previsic, *Cost Breakdown Structure for WEC Rated at 286 kW*, 2012.

[19] ME Ochs, DL Bull, DL Laird, RA Jepsen, and B Boren, *Technological Cost-Reduction Pathways for Point Absorber Wave Energy Converters in the Marine Hydrokinetic Environment.* SAND2013-7204, 1092993 (Sept. 1, 2013), SAND2013–7204, 1092993, 10.2172/1092993.

[20] G Rinaldi, JCC Portillo, F Khalid, JCC Henriques, PR Thies, LMC Gato, and L Johanning, "Multivariate analysis of the reliability, availability, and maintainability characterizations of a Spar–Buoy wave energy converter farm", Journal of Ocean Engineering and Marine Energy **4**, 199–215 (2018) 10.1007/s40722-018-0116-z.

[21] MB Topper, V Nava, AJ Collin, D Bould, F Ferri, SS Olson, AR Dallman, JD Roberts, P Ruiz-Minguela, and HF Jeffrey, "Reducing variability in the cost of energy of ocean energy arrays", Renewable and Sustainable Energy Reviews **112**, 263–279 (2019) 10.1016/j.rser.2019.05.032.

[22] S Ambühl, L Marquis, JP Kofoed, and J Dalsgaard Sørensen, "Operation and maintenance strategies for wave energy converters", Proceedings of the Institution of Mechanical Engineers, Part O: Journal of Risk and Reliability **229**, 417–441 (2015) 10.1177/1748006X15577877.

[23] S Astariz and G Iglesias, "The economics of wave energy: A review", Renewable and Sustainable Energy Reviews **45**, 397–408 (2015) 10.1016/j.rser.2015.01.061.

[24] MM Kramer, L Marquis, and P Frigaard, "Performance Evaluation of the Wavestar Prototype", 10.

[25] JP Kofoed, P Frigaard, E Friis-Madsen, and HC Sørensen, "Prototype testing of the wave energy converter wave dragon", Renewable Energy **31**, 181–189 (2006) 10.1016/j.renene.2005.09.005.

[26] B Teillant, R Costello, J Weber, and J Ringwood, "Productivity and economic assessment of wave energy projects through operational simulations", Renewable Energy **48**, 220–230 (2012) 10.1016/j.renene.2012.05.001.

[27] J van Rij, YH Yu, and Y Guo, "Structural Loads Analysis for Wave Energy Converters", in Volume 10: Ocean Renewable Energy (June 25, 2017), V010T09A023, 10.1115/OMAE2017-62139.

[28] S Yang, "Analysis of the Fatigue Characteristics of Mooring Lines and Power Cables for Floating Wave Energy Converters", 114.

[29] van Rij, Yu, Guo, and Coe, "A Wave Energy Converter Design Load Case Study", Journal of Marine Science and Engineering **7**, 250 (2019) 10.3390/jmse7080250.

[30] Robert G Dean and Robert A Dalrymple, *Water Wave Mechanics for Engineers and Scientists* (Prentice-Hall, Englewood Cliffs, N.J., 1984).

[31] JN Newman, "Algorithms for the free-surface Green function", Journal of Engineering Mathematics **19**, 57–67 (1985) 10.1007/BF00055041.

[32] M Ancellin and F Dias, "Capytaine: a Python-based linear potential flow solver", Journal of Open Source Software **4**, 1341 (2019) 10.21105/joss.01341.

[33] A Babarit and G Delhommeau, "Theoretical and numerical aspects of the open source BEM solver NEMOH", in Proceedings of the 11th European Wave and Tidal Energy Conference (EWTEC2015) (2015).

[34] J NEWMAN and P Sclavounos, "The computation of wave loads on large offshore structures", in Boss'88 (1988), pp. 605–622.

[35] JV Ringwood, "Wave energy control: status and perspectives 2020", 13.

[36] J Newman, "Wave effects on deformable bodies", Applied Ocean Research **16**, 47–59 (1994) 10.1016/0141-1187(94)90013-2.

[37] Z. Yu and J. Falnes, "State-space modelling of a vertical cylinder in heave", Applied Ocean Research **17**, 265–275 (1995).

[38] B Bosma, Z Zhang, TK Brekken, HT Ozkan-Haller, C McNatt, and SC Yim, "Wave energy converter modeling in the frequency domain: A design guide", in 2012 IEEE Energy Conversion Congress and Exposition (ECCE) (Sept. 2012), pp. 2099–2106, 10.1109/ECCE.2012.6342553.

[39] W Cummins, *The impulse response function and ship motions*, tech. rep. (David Taylor Model Basin Washington DC, 1962).

[40] R Taghipour, T Perez, and T Moan, "Hybrid frequency–time domain models for dynamic response analysis of marine structures", Ocean Engineering **35**, 685–705 (2008) 10.1016/j.oceaneng.2007.11.002.

[41] JA Armesto, R Guanche, F Del Jesus, A Iturrioz, and IJ Losada, "Comparative analysis of the methods to compute the radiation term in cummins' equation", Journal of Ocean Engineering and Marine Energy **1**, 377–393 (2015).

[42] MP Retes, G Giorgi, and JV Ringwood, "A Review of Non-Linear Approaches for Wave Energy Converter Modelling", 10.

[43] MP Retes, A Merigaud, JC Gilloteaux, and JV Ringwood, "Nonlinear Froude-Krylov force modelling for two heaving wave energy point absorbers", 10.

[44] YH Yu, M Lawson, Y Li, M Previsic, J Epler, and J Lou, *Experimental Wave Tank Test for Reference Model 3 Floating-Point Absorber Wave Energy Converter Project*, NREL/TP–5000-62951, 1169792 (Jan. 1, 2015), NREL/TP–5000–62951, 1169792, 10.2172/1169792.

[45] A Babarit, F Wendt, YH Yu, and J Weber, "Investigation on the energy absorption performance of a fixed-bottom pressure-differential wave energy converter", Applied Ocean Research **65**, 90–101 (2017) 10.1016/j.apor.2017.03.017.

[46] A Babarit, B Gendron, J Singh, C Mélis, and P Jean, "Hydro-Elastic Modelling of an Electro-Active Wave Energy Converter", in Volume 9: Odd M. Faltinsen Honoring Symposium on Marine Hydrodynamics (June 9, 2013), V009T12A033, 10.1115/OMAE2013-10848.

[47] Reza Taghipour, Tristan Perez, and Torgeir Moan, "Time-Domain Hydroelastic Analysis of a Flexible Marine Structure Using State-Space Models", Journal of Offshore Mechanics and Arctic Engineering **131** (2009).

[48] A Babarit, J Singh, C Mélis, A Wattez, and P Jean, "A linear numerical model for analysing the hydroelastic response of a flexible electroactive wave energy converter", Journal of Fluids and Structures **74**, 356–384 (2017) 10.1016/j.jfluidstructs.2017.06.003.

[49] A. McDonald, Q. Xiao, D.I.M. Forehand, H. Smith, and R. Costello, "Initial development of a generic method for analysis of flexible membrane wave energy converters", Advances in Renewable Energies Offshore: Proceedings of the 3rd International Conference on Renewable Energies Offshore (RENEW 2018), 333–340 (2019).

[50] Y Guo and YH Yu, "Inclusion of Structural Flexibility in Design Load Analysis for Wave Energy Converters", 8.

[51] J van Rij, YH Yu, and RG Coe, "Design Load Analysis for Wave Energy Converters", in Volume 10: Ocean Renewable Energy (June 17, 2018), V010T09A031, 10.1115/OMAE2018-78178.

[52] J Scriven, P Laporte-Weywada, and J Cruz, "Introducing non-rigid body structural dynamics to WEC-Sim", International Marine Energy Journal **3**, 55–63 (2020) 10.36688/imej.3.55-63.

[53] S Ambühl, M Kramer, and J Sørensen, "Reliability-Based Structural Optimization of Wave Energy Converters", Energies **7**, 8178–8200 (2014) 10.3390/en7128178.

[54] PM Singh, Z Chen, and YD Choi, "Component structural analysis on 15kW class wave energy converter", Journal of the Korean Society of Marine Engineering **39**, 821–827 (2015) 10.5916/jkosme.2015.39.8.821.

[55] M Lawson, YH Yu, K Ruehl, C Michelen, et al., "Development and demonstration of the wec-sim wave energy converter simulation tool", (2014).

[56] LD Rosen, "(76) Inventors: Jack Pollack, Camarillo, CA (US); Philippe F. Jean, Nice (FR)", 10.

[57] J Falnes, "OPTIMUM CONTROL OF OSCILLATION OF WAVE-ENERGY CONVERTERS", 12.

[58] AAE Price, "New Perspectives on Wave Energy Converter Control", 319.

[59] Y Hong, R Waters, C Boström, M Eriksson, J Engström, and M Leijon, "Review on electrical control strategies for wave energy converting systems", Renewable and Sustainable Energy Reviews **31**, 329–342 (2014) https://doi.org/10.1016/j.rser.2013.11.053.

[60] David N. Glennon, "Design and Simulation of Nonlinear Control Strategies for Heaving Point Wave Energy Converters in WEC-Sim" (Oregon State University, 2019).

[61] CE Clark, A Garcia-Teruel, B DuPont, and D Forehand, "Towards reliability-based geometry optimization of a point-absorber with PTO reliability objectives", 10.

[62] SJ Edwards, "The Effect of Environmental Contour Selection on Expected WEC Response", 24.

[63] M Hall and A Goupee, "Validation of a lumped-mass mooring line model with DeepCwind semisubmersible model test data", Ocean Engineering **104**, 590–603 (2015) 10.1016/j.oceaneng.2015.05.035.

[64] PTT Nguyen, L Manuel, and RG Coe, "On the Development of an Efficient Surrogate Model for Predicting Long-Term Extreme Loads on a Wave Energy Converter", Journal of Offshore Mechanics and Arctic Engineering **141**, 061103 (2019) 10.1115/1.4042944.

[65] G Bacelli, "Optimal control of wave energy converters", 218.

[66] G Bacelli and RG Coe, "Comments on Control of Wave Energy Converters", IEEE Transactions on Control Systems Technology, 1–4 (2020) 10.1109/TCST.2020.2965916.

[67] A Stock, N Tom, and C Gonzalez, "Adapting Optimal Velocity Tracking Control To Account for WEC Constraints and Power-Take-Off Efficiencies: Preprint", Renewable Energy, 9 (2020).

[68] GA Nolan, JV Ringwood, WE Leithead, and S Butler, "Optimal Damping Profiles for a Heaving Buoy Wave Energy Converter", 8.

[69] G Li and MR Belmont, "Model predictive control of sea wave energy converters – Part I: A convex approach for the case of a single device", Renewable Energy **69**, 453–463 (2014) 10.1016/j.renene.2014.03.070.

[70] A Stock and C Gonzalez, "Design of optimal velocity tracking controllers for one and two-body point absorber wave energy converters", Renewable Energy **162**, 1563–1575 (2020) 10.1016/j.renene.2020.09.102.

[71] E Anderlini, S Husain, GG Parker, M Abusara, and G Thomas, "Towards Real-Time Reinforcement Learning Control of a Wave Energy Converter", Journal of Marine Science and Engineering **8**, 845 (2020) 10.3390/jmse8110845.

[72] R Henderson, "Design, simulation, and testing of a novel hydraulic power take-off system for the Pelamis wave energy converter", Renewable Energy **31**, 271–283 (2006) 10.1016/j.renene.2005.08.021.

[73] R Hansen, M Kramer, and E Vidal, "Discrete Displacement Hydraulic Power Take-Off System for the Wavestar Wave Energy Converter", Energies **6**, 4001–4044 (2013) 10.3390/en6084001.

[74] LM Yang, J Hals, and T Moan, "A wear model for assessing the reliability of wave energy converter in heave with hydraulic power take-off", 9.

[75] F Ferri, S Ambühl, B Fischer, and J Kofoed, "Balancing Power Output and Structural Fatigue of Wave Energy Converters by Means of Control Strategies", Energies **7**, 2246–2273 (2014) 10.3390/en7042246.

[76] N Tom, Y Yu, A Wright, and M Lawson, "Pseudo-spectral control of a novel oscillating surge wave energy converter in regular waves for power optimization including load reduction", Ocean Engineering **137**, 352–366 (2017) 10.1016/j.oceaneng.2017.03.027.

[77] RG Coe and VS Neary, "Review of Methods for Modeling Wave Energy Converter Survival in Extreme Sea States", 8.

[78] A Brown, R Paasch, IY Tumer, P Lenee-Bluhm, J Hovland, A von Jouanne, and T Brekken, "Towards a Definition and Metric for the Survivability of Ocean Wave Energy Converters", in ASME 2010 4th International Conference on Energy Sustainability, Volume 1 (2010), pp. 917–927, 10.1115/ES2010-90069.

[79] T Mundon and B Rosenberg, "Development of a Survival Configuration for the Triton Wave Energy Converter", 5.

[80] T Stallard, S Weller, and P Stansby, "Limiting heave response of a wave energy device by draft adjustment with upper surface immersion", Applied Ocean Research **31**, 282–289 (2009) 10.1016/j.apor.2009.08.001.

[81] CE Larsen and T Irvine, "A Review of Spectral Methods for Variable Amplitude Fatigue Prediction and New Results", Procedia Engineering **101**, 243–250 (2015) 10.1016/j.proeng.2015.02.034.

[82] P Ragan and L Manuel, "Comparing estimates of wind turbine fatigue loads using time-domain and spectral methods", Wind engineering **31**, 83–99 (2007).

[83] H Ding, Q Zhu, and P Zhang, "Fatigue damage assessment for concrete structures using a frequency-domain method", Mathematical Problems in Engineering **2014** (2014).

[84] J Xu, Y Zhang, Q Han, J Li, and G Lacidogna, "Research on the scope of spectral width parameter of frequency domain methods in random fatigue", Applied Sciences **10**, 4715 (2020).

[85] M Ancellin, M Dong, P Jean, and F Dias, "Far-field maximal power absorption of a bulging cylindrical wave energy converter", Energies **13**, 10.3390/en13205499 (2020) 10.3390/en13205499.

[86] M Kochenderfer and T Wheeler, *Algorithms for optimization* (The MIT Press, Cambridge, Massachusetts, 2019).

[87] B Boren, T Mathai, S Sirnivas, and R Preus, *Internal report on evaluation of cost and performance drivers: key cost and performance drivers identified and approximately quantified*, Sept. 2021.

[88] O Faltinsen, "Sea loads on ships and offshore structures",

[89] *Structural Loads Analysis for Wave Energy Converters*, Vol. Volume 10: Ocean Renewable Energy, International Conference on Offshore Mechanics and Arctic Engineering, V010T09A023 (June 2017), 10.1115/OMAE2017-62139.

[90] J van Rij, YH Yu, Y Guo, and RG Coe, "A wave energy converter design load case study", Journal of Marine Science and Engineering **7**, 10.3390/jmse7080250 (2019) 10.3390/jmse7080250.

[91] A Babarit, J Singh, C Mélis, A Wattez, and P Jean, "A linear numerical model for analysing the hydroelastic response of a flexible electroactive wave energy converter", Journal of Fluids and Structures **74**, 356–384 (2017) 10.1016/j.jfluidstructs.2017.06.003.

[92] P Virtanen, R Gommers, TE Oliphant, M Haberland, T Reddy, D Cournapeau, E Burovski, P Peterson, W Weckesser, J Bright, SJ van der Walt, M Brett, J Wilson, KJ Millman, N Mayorov, ARJ Nelson, E Jones, R Kern, E Larson, CJ Carey, bibinitperiodI Polat, Y Feng, EW Moore, J VanderPlas, D Laxalde, J Perktold, R Cimrman, I Henriksen, EA Quintero, CR Harris, AM Archibald, AH Ribeiro, F Pedregosa, P van Mulbregt, and SciPy 1.0 Contributors, "SciPy 1.0: Fundamental Algorithms for Scientific Computing in Python", Nature Methods **17**, 261–272 (2020) 10.1038/s41592-019-0686-2.

[93] A Dallman and V Neary, *Characterization of u.s. wave energy converter (wec) test sites: a catalogue of met-ocean data* (Jan. 2014).

[94] J van Rij, YH Yu, B Boren, J Weber, and A Cardinal, *Internal report on numerical system model implementation: models are fit for purpose, & internal report on system simulation results*, Sept. 2021.

[95] PI Frazier, *A tutorial on bayesian optimization*, 2018.

[96] J Jiménez and J Ginebra, "Pygpgo: bayesian optimization for python", Journal of Open Source Software **2**, 431 (2017) 10.21105/joss.00431.